Experimental study of nearshore dynamics on a barred beach with rip channels

Merrick C. Haller[1]
Cooperative Institute for Limnology and Ecosystems Research, University of Michigan, Ann Arbor, Michigan, USA

Robert A. Dalrymple and Ib A. Svendsen
Center for Applied Coastal Research, University of Delaware, Newark, Delaware, USA

Received 4 May 2001; revised 17 October 2001; accepted 6 November 2001; published 28 June 2002.

[1] Wave and current measurements are presented from a set of laboratory experiments performed on a fixed barred beach with periodically spaced rip channels using a range of incident wave conditions. The data demonstrate that the presence of gaps in otherwise longshore uniform bars dominates the nearshore circulation system for the incident wave conditions considered. For example, nonzero cross-shore flow and the presence of longshore pressure gradients, both resulting from the presence of rip channels, are not restricted to the immediate vicinity of the channels but instead are found to span almost the entire length of the longshore bars. In addition, the combination of breaker type and location is the dominant driving mechanism of the nearshore flow, and both are found to be strongly influenced by the variable bathymetry and the presence of a strong rip current. The depth-averaged currents are calculated from the measured velocities assuming conservation of mass across the measurement grid. The terms in both the cross-shore and longshore momentum balances are calculated, and their relative magnitudes are quantified. The cross-shore balance is shown to be dominated by the cross-shore pressure and radiation stress gradients in general agreement with previous results, however, the rip current is shown to influence the wave breaking and the wave-induced setup in the rip channel. Analysis of the longshore balance shows that the overall strength of the longshore feeder currents is governed by a balance between longshore pressure gradient forcing and an opposing radiation stress gradient. In addition, the longshore feeder currents show maxima in the bar trough region, providing experimental evidence that longshore pressure gradients can shift longshore current maxima shoreward from the bar crest. Finally, since the longshore radiation stress gradient in the surf zone is governed by the amount of wave dissipation on the rip current, there exists a positive feedback mechanism whereby a strong rip current can weaken the radiation stress gradient opposing the feeder currents and lead to even stronger feeder currents and rips. *INDEX TERMS:* 4546 Oceanography: Physical: Nearshore processes; 4512 Oceanography: Physical: Currents; 4560 Oceanography: Physical: Surface waves and tides (1255); *KEYWORDS:* nearshore, rip current, longshore current, sand bar, rip channel

1. Introduction

[2] Rip channels are local depressions in the nearshore bathymetry that are created by the erosive action of strong offshore-directed flows called rip currents. These currents have been observed on a wide range of beach types but are particularly common on beaches that are dominated by a longshore bar-trough morphology [*Wright and Short*, 1984]. In general, rip currents are contained within coherent nearshore circulation cells that are driven by periodic longshore variations in the incident wave field [e.g., *Bowen*, 1969]. These longshore variations in the incident wave field may arise on an initially longshore uniform beach owing to a wide range of causes including edge waves [*Bowen and Inman*, 1969], the superposition of wave trains [*Dalrymple*, 1975; *Fowler and Dalrymple*, 1990], or surf zone instabilities [*Dalrymple and Lozano*, 1978; *Falqués et al.*, 1999]. However, as the rips erode distinct rip channels, the necessary longshore variability in wave height becomes topographically controlled, and therefore the circulation can remain long after the initial source of variability has diminished [*McKenzie*, 1958]. In fact, *Aagaard et al.* [1997] report observations from the coast of Denmark, which indicate the existence of rip channels and longshore bars that remain stationary for periods of several months.

[1]Now at Department of Civil, Construction, and Environmental Engineering, Oregon State University, Corvallis, USA.

0148-0227/02/2001JC000955

[3] The influence of rip currents on nearshore circulation has been observed qualitatively in the field for many decades now [see *Shepard et al.*, 1941; *Shepard and Inman*, 1950]. It is evident that the presence and persistence of rip currents modifies the incident wave environment, the circulation of water in the surf zone, the magnitude and direction of sediment transport, and, ultimately, the shape of the coastline. Since rip currents serve as highly efficient drainage conduits that release back to sea water that is first brought shoreward and piled up on the beach by breaking waves, the size, number, and location of rips are influenced by the ambient wave conditions. *McKenzie* [1958], citing observations made on sandy Australian beaches, noted that rip currents are generally absent under very low wave conditions but are more numerous and somewhat larger under light to moderate swell. With increasing wave conditions the increased volume of water moving shoreward requires the rips to grow in size and activity. These observations suggest a direct relationship between rip current flows and wave-forcing parameters, and this relationship has important consequences for the nearshore sediment budget and beach profile equilibrium, since variations in current strength will significantly affect the erosional power of rips.

[4] Field observations have also shown the influence of tides on rip currents. *Cooke* [1970] conducted a study at Redondo Beach, California, that concentrated on the role of rip currents in the nearshore sediment transport system. He noted that at this site, stationary rip channels were commonly present, but well-defined rip currents were only present during falling or low tides. The prevalence of rip currents during falling tides was also noted by *McKenzie* [1958] and was attributed to the concentration of the drainage system into the current channels, resulting in stronger current flows.

[5] Despite the qualitative knowledge of the importance of rip currents in the nearshore circulation, a comprehensive data set of nearshore circulation in the presence of rip currents is not presently available. Since, in the field, rip currents are often transient, they tend to elude investigators intent on measuring them with stationary instrument deployments, though quantitative measurements do exist [e.g., *Sonu*, 1972; *Bowman et al.*, 1988a, 1988b; *Aagaard et al.*, 1997; *Brander and Short*, 2000]. However, because of the large scales of rip circulation systems and the difficult nature of rip observations, field studies have as yet been unable to obtain a comprehensive map of water surface elevations and currents in rip systems under a range of wave conditions. Instead, most field studies have concentrated on the morphologic evolution of the beach in the presence of rip currents, and the measured current data are generally sparse and limited to very near the rip current. It is clear that a comprehensive rip current data set will aid in the improved understanding of the overall hydrodynamics of rip systems and is needed in order to make further advances in predicting their sediment transport characteristics.

[6] The controlled environment of the laboratory is ideal for studying rip current systems. The extent of laboratory data involving rip currents on longshore-varying bathymetry is limited to two brief studies [*Hamm*, 1992; *Drønen et al.*, 1999]. To the authors' knowledge, the present study is the first that provides a comprehensive map of the nearshore waves and currents, including the details of the mean water level variations, on a barred bathymetry with multiple rip channels combined with a quantitative analysis of the nearshore momentum balances calculated from the measurements.

[7] In section 2 we describe the physical model and the experimental conditions. In section 3 we will present maps of the nearshore circulation and demonstrate that the longshore variability of the bathymetry and the current field significantly affects the nature and location of wave breaking. By applying the conservation of mass across the measurement grid, we calculate the depth-averaged current fields and show that the presence of the rip channels influences the nearshore circulation system along the entire bar-channel system. In section 4 we calculate the cross-shore and longshore momentum balances. The balances in both directions are shown to be dominated by gradients in pressure and radiation stress; however, the influence of an opposing rip current on the wave dissipation in the rip channel is also shown to significantly influence the nearshore dynamics. The results are summarized in section 5.

2. Experimental Setup

2.1. Physical Model

[8] The laboratory experiments were performed in the directional wave basin located in the Ocean Engineering Laboratory at the University of Delaware. A plan view and a cross section of the wave basin are shown in Figures 1a and 1b, respectively. Figure 1a also shows the coordinate axes; the origin is located in one corner where the wave maker and one sidewall meet. The internal dimensions of the wave basin are approximately 17.2 m in length and 18.2 m in width, and the wave maker consists of 34 paddles of flap type. The beach consists of a steep (1 : 5) toe located between 1.5 m and 3 m from the wave maker with a milder (1 : 30) sloping section extending from the toe to the wall of the basin opposite the wave maker. Three ''sandbar'' sections were constructed in the shape of a generalized bar profile from sheets of high-density polyethylene (HDP). The completed bar system consisted of three sections: one main section spanning approximately 7.32 m longshore and two half-sections spanning approximately 3.66 m (longshore) each. In order to insure that the sidewalls were located along lines of symmetry, the longest section was centered in the middle of the tank, and the two half-sections were placed against the sidewalls. This left two gaps of approximately 1.82 m width, centered at 1/4 and 3/4 of the basin width, that served as rip channels. The edges of the bars on each side of the gaps were rounded off with cement in order to limit wave reflections. After each bar section was completed, all exposed joints and the contacts between the HDP and the beach were sealed with caulking meant for underwater use. After all the bar sections were installed, the bathymetry was accurately measured using survey equipment. The seaward edges of the bar sections were located at approximately $x = 11.1$ m with the bar crest at $x = 12$ m and their shoreward edges at $x = 12.3$ m.

[9] The experimental setup was not designed to be an exact replica of a particular field beach; however, it is

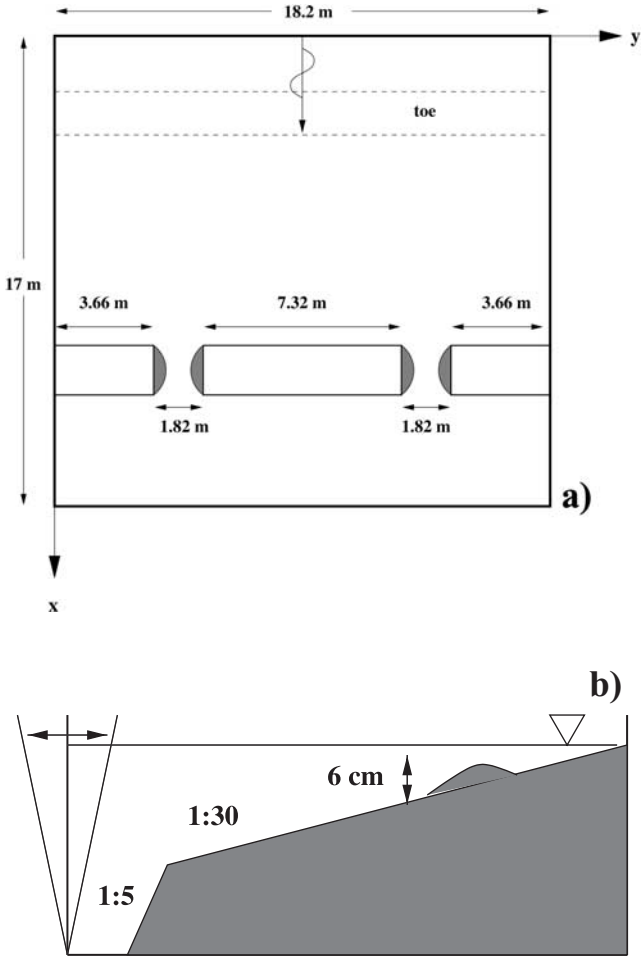

Figure 1. (a) Plan view and (b) cross section of the experimental basin.

important to note that the present bar-trough geometry is a reasonable approximation of similar beach types observed in the field. Depending on the still water level for a given test, the ratio of rip current spacing to surf zone width varied between 2.7 and 4.0 during these experiments, which falls within the range of 1.5 to 8.0 estimated by *Huntley and Short* [1992] from a large data set of field observations. Another ratio of interest is rip channel width to rip current spacing. During these experiments this ratio was fixed at 1/5; this also compares favorably with the field observations of *Aagaard et al.* [1997] and *Brander and Short* [2000]. Finally, if we consider the experiments as an undistorted Froude model of field conditions with a length scale ratio of 1/50, then the experimental conditions correspond to a rip spacing of 450 m, rip channel width of 90 m, breaking wave heights of 1.3–3.8 m, wave periods of 5.7–7.1 s, and mean offshore velocities of 1.0–2.1 m/s in the rip neck.

2.2. Data Collection

[10] Ten capacitance wave gauges were used to measure time series of water surface elevation during the experiments. These gauges have nearly linear response of output voltage versus water level at the gauge wire and performed well during the experiments. The wave gauges were calibrated quite often. Usually, they were calibrated every morning and repeatedly during the day whenever the gauges were moved. Nine gauges were mounted on a mobile carriage that spanned the basin in the longshore direction; the tenth gauge was mounted on a separate quadripod which moved around the basin to provide offshore reference measurements.

[11] Three two-dimensional side-looking acoustic Doppler velocimeters (ADVs) were used to obtain time series of horizontal currents. These probes are designed to work in water depths as small as 3 cm and are hardwired to a dedicated PC for data acquisition. This PC was linked, also by cable, to the mainframe that acquired the wave data, so that the onset of data acquisition for all sensors was synchronized. The ADVs do not require calibration, and a mounting system was designed that allowed them to be mounted either on the beam holding the wave gauges or on separate aluminum box beams that could be oriented in both the x and y directions and rigged to the carriage at various locations.

[12] For all experimental runs, data were sampled at 10 Hz by all sensors, and data acquisition was started at or very near the onset of wave generation. During wave generation, 16,384 data points were sampled by each sensor, except for a few tests of longer duration. For this analysis, the first 1024 points of all wave and velocity data were removed before processing in order to remove wave maker startup effects. Individual wave heights were determined from the water surface elevation records using a zero-up crossing method and then averaged to determine the mean.

[13] As the experimental work proceeded, the measuring location plan for all the sensors evolved. The locations of the wave gauges and the ADVs are shown in Figures 2–3 for all tests. The first test (test B) contains the most extensive spatial map of currents. This test, in addition to earlier pilot experiments, suggested that the circulation fields associated with the two rip currents were reasonably equivalent and behaving independently; therefore the measurements were concentrated into one half of the basin. The subsequent test (test C) concentrated on measuring the flow field of one of the rip currents in detail, and the remaining tests (tests D–G) obtained general velocity measurements in the longshore current and in the rip. All tests contain a reasonably extensive map of the wave heights since there were many more wave gauges, whereas the current measurements were always at a premium because of the lack of sensors. In general, the ADV measurements were made 3 cm from the bottom, but certain offshore measurements were made at locations higher in the water column.

[14] The total water depth in the basin was measured by a depth gauge located near the wave paddles. This gauge was demarcated at 0.1 mm intervals; however, the total water level in the basin could vary ±1 mm from run to run. For further information regarding the experimental procedures (the entire data set is publicly available via ftp from the Center for Applied Coastal Research, University of Delaware) and the model basin the reader is referred to *Haller et al.* [2000].

2.3. Wave Conditions

[15] The test conditions typically consisted of monochromatic, normally incident waves with a period of 1 s, except for test E (0.8 s period) and test F (10° incidence). Specific

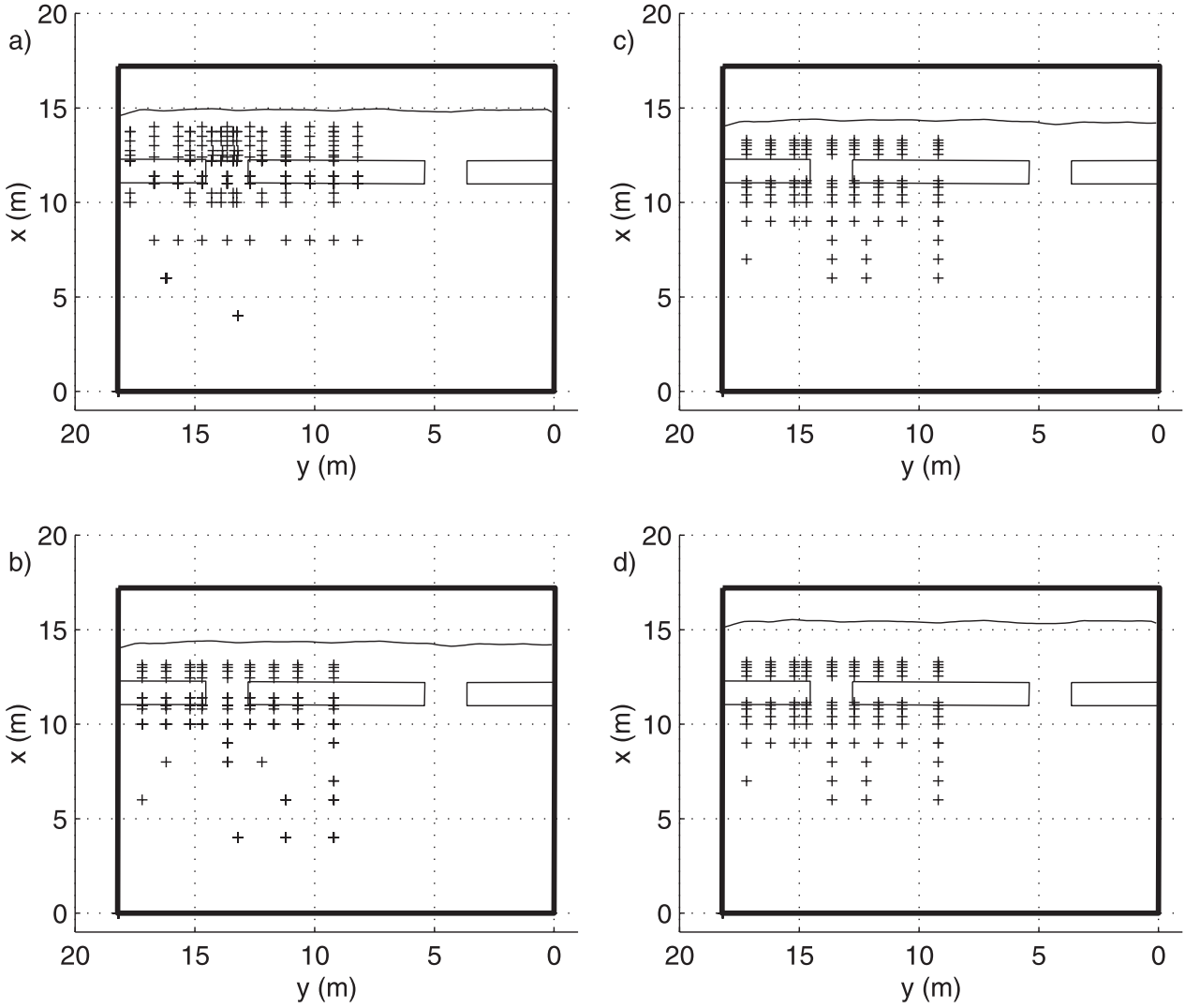

Figure 2. Wave gauge sampling locations for (a) test B, (b) test C, (c) tests D–F, and (d) test G; the still water shoreline is shown as the solid line near x = 15 m.

parameters such as wave height near the crest of the center bar, equivalent deep water wave height (calculated from linear theory), wave period, incident angle, water depth at the bar crest, shoreline location, and mean rip velocity are given in Table 1. The tests can be divided into two categories: (1) varying wave forcing with constant water depth (tests E, C, and D) and (2) similar wave forcing with varying water depths (tests B and G). A final test (test F) considered waves incident at a slightly oblique angle.

[16] The regular waves were generated using the (linear) theory of *Dalrymple* [1989] assuming longshore uniformity. The mean beach profile used for the wave generation code was obtained by averaging cross-shore transects from the survey data that contained the bars. For all the tests the wave maker theory was used to generate a uniform plane wave of target amplitude at the seaward edge of the bar system. For test F the wave maker theory was designed to utilize sidewall reflections in order to generate a uniform obliquely incident wave train at x = 11 m. Typically, the criterion of a uniform plane wave offshore of the bars was fairly well met. However, certain small longshore variations in the offshore wave height were evident during all tests. Some of these variations were attributed to a longshore modulation in the beach due to settling of the concrete, especially at the centerline of the tank. Also, smaller-scale variations in the amplitude were present and became more pronounced with increasing offshore wave height. These can be attributed to several factors, including nonlinear wave effects, noise due to the gaps between paddles, and high-frequency basin seiche modes.

[17] Since it was necessary to repeat a given test a number of times in order to obtain an extensive spatial map of the current fields, it was important to estimate the repeatability of the test conditions. Since there were many more wave gauges than ADVs, it was possible to repeat a number of wave measurements at the same location and under the same specified wave conditions. A statistical analysis of the repeated measurements (see Appendix A) demonstrated very little variability offshore of the surf zone with variability increasing in the surf zone especially within

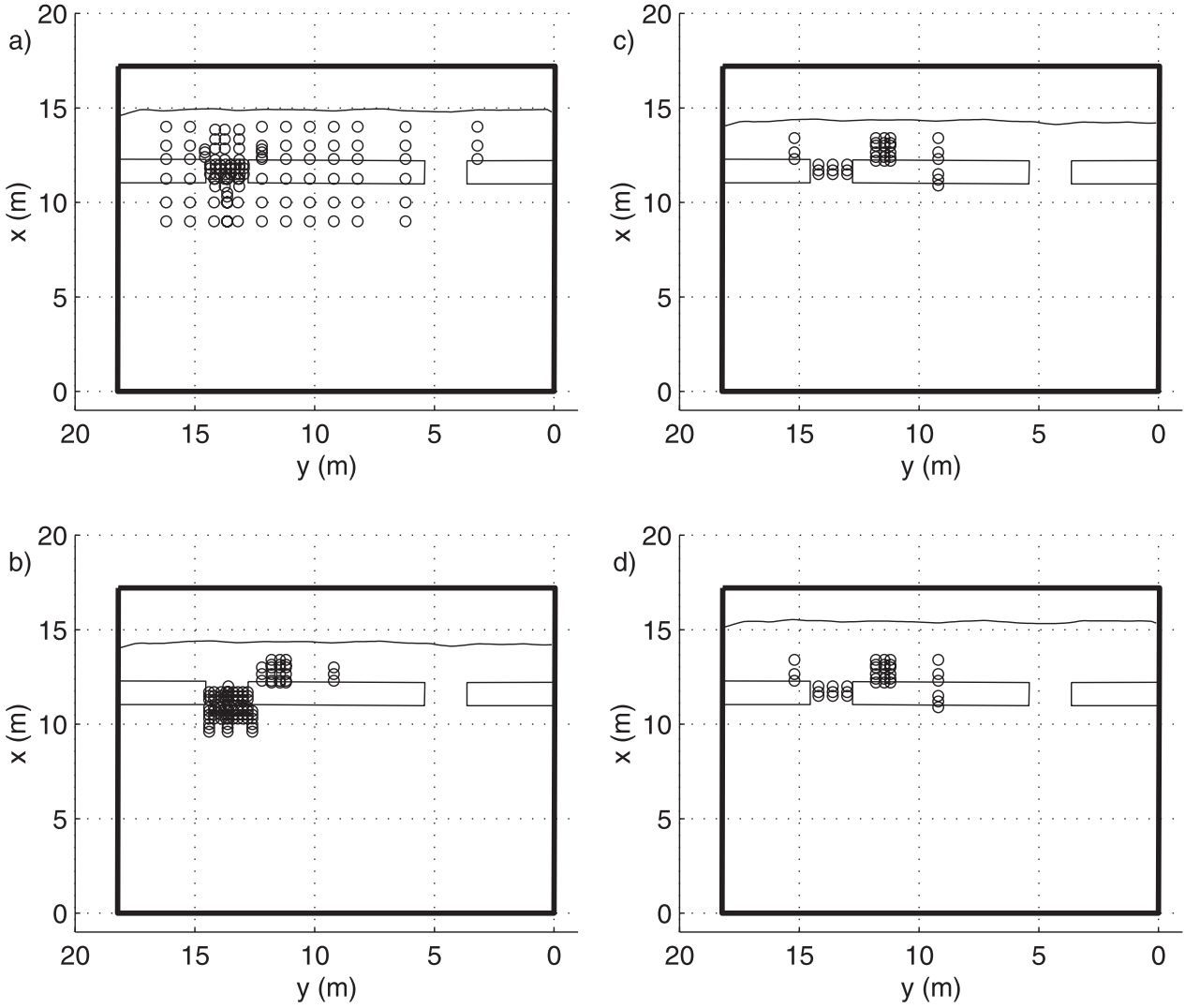

Figure 3. Current meter sampling locations for (a) test B, (b) test C, (c) tests D–F, and (d) test G; the still water shoreline is shown as the solid line near x = 15 m.

~1 m of the rip currents. On the basis of the measuring locations with the highest variability it is estimated that deviation of the mean wave heights was always less than ~4% with most locations deviating by less than 2%. The deviations of the mean water line (MWL) were always less than ~0.02 cm and generally less than 0.01 cm. Other sources of experimental error include spatial errors due to inexact positioning of the sensors; these errors are estimated to be less than 1 cm and lead to a corresponding uncertainty in the still water depth of less than ±0.04 cm. Also, the position of the ADVs relative to the bottom is estimated to be accurate within 0.5 cm.

3. Results

3.1. Overview

[18] The nearshore dynamics are dominated by the presence of the bars and rip channels on this experimental beach. A common feature of all the tests was the contrast between the wave evolution observed through the rip channels and that observed over the bars. The incident long-crested waves formed steep plunging breakers as they propagated over the bars, and the breaking on the bars was confined to a fairly narrow region (11.8 m < x < 12.4 m). There was minor reshoaling in the bar troughs and an

Table 1. Table of Experimental Conditions[a]

Test	H_{bar}, cm	H_0, cm	T, s	θ deg, cm	h_c, cm	x_{swl}, cm	U_r, cm/s
E	4.17	4.52	0.8	0	2.67	1430	14.33
C	4.94	5.22	1.0	0	2.67	1430	18.82
D	7.56	8.26	1.0	0	2.67	1430	30.33
B	4.41	5.12	1.0	0	4.73	1490	14.2
G	6.79	7.43	1.0	0	6.72	1540	15.91
F	2.63	3.59	1.0	10	2.67	1430	19.94

[a] Wave height H_{bar} measured near the offshore edge of the center bar (x = 10.92 m, y = 9.23 m), deepwater wave height H_0, wave period T, angle of incidence θ (positive angles indicate that the wave propagation direction has a component in the positive y direction), average water depth at the bar crest h_c, cross-shore location of the still water line x_{swl}, and the mean (averaged in time and in y) rip velocity U_r measured at the rip neck.

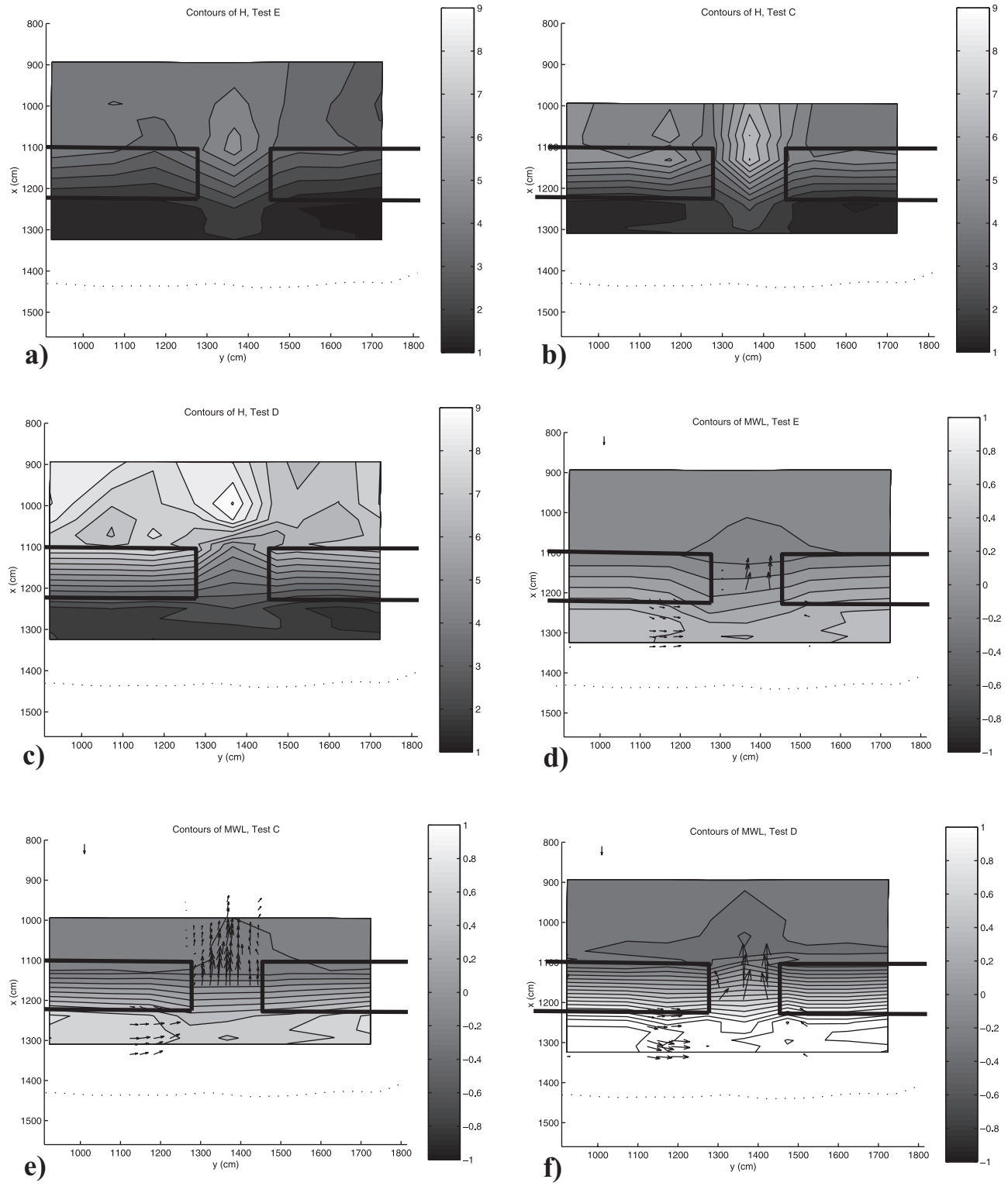

Figure 4. (a–c) Contours of wave height (interval 0.5 cm) and (d–f) contours of MWL (interval 0.1 cm) with vectors of mean currents. Vector at upper left equals 10 cm/s and is shown for scale; still water shoreline is shown as dotted line.

additional narrow breaking region very near the shoreline. In contrast, as the waves approached the rips, they steepened faster owing to the presence of the opposing current. As the waves propagate through the channel, the breaking is often less intense compared to the rapid breaking over the bars. However, if the rip current is of sufficient strength, the wave breaking in the channel can be equally as intense as that over the bar.

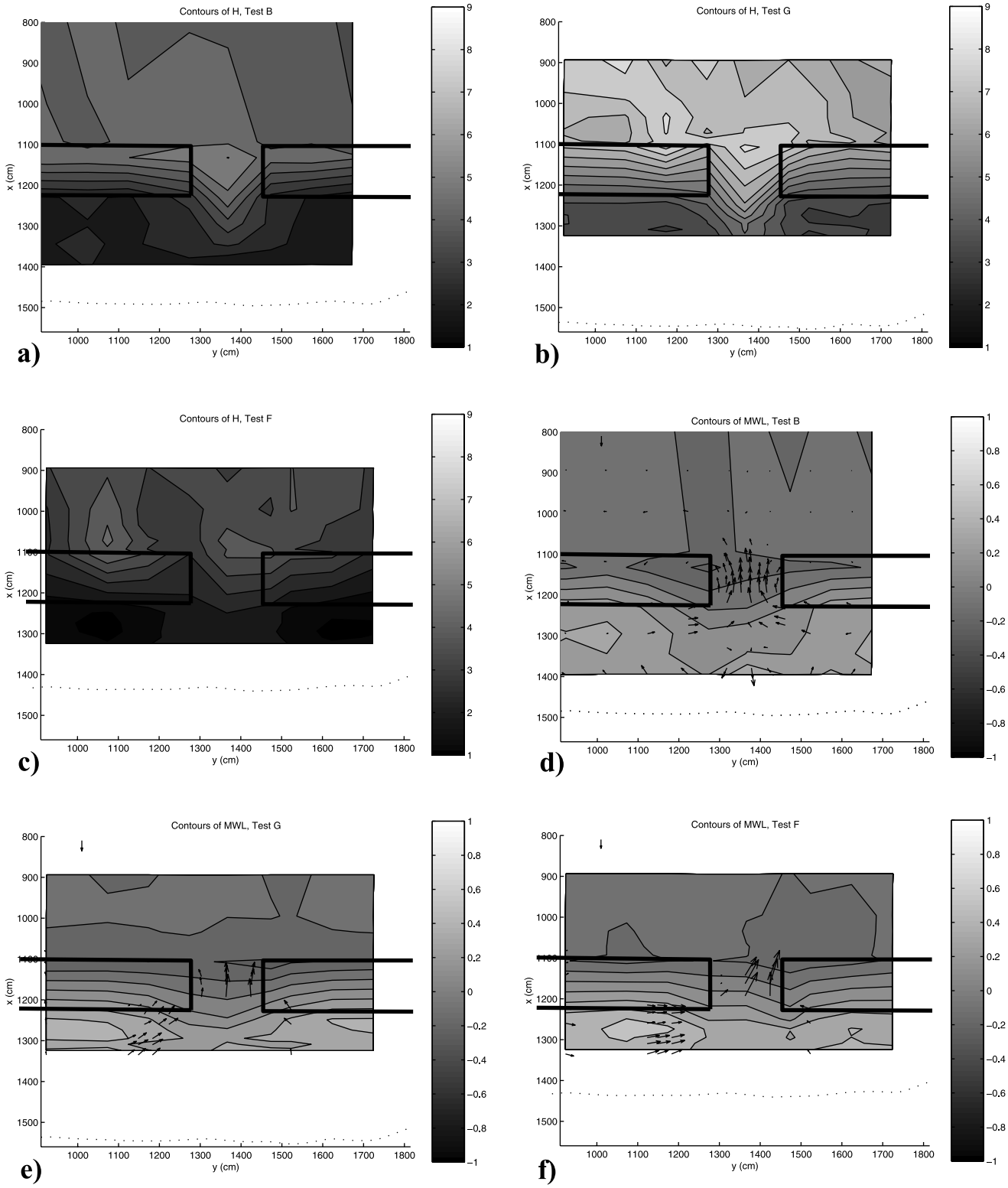

Figure 5. (a–c) Contours of wave height (interval 0.5 cm) and (d–f) contours of MWL (interval 0.1 cm) with vectors of mean currents. Vector at upper left equals 10 cm/s and is shown for scale; still water shoreline is shown as dotted line.

[19] Figures 4–5 show the spatial variability of wave height and MWL measured during all the tests. Offshore of the breaking regions, there is slightly larger wave setdown near the rip channel because of the larger wave heights in that region. Shoreward of the bars, longshore variations in wave setup are present owing to the stronger breaking on the bars, which raises the water level in the trough region and causes the MWL to slope downward toward the rip

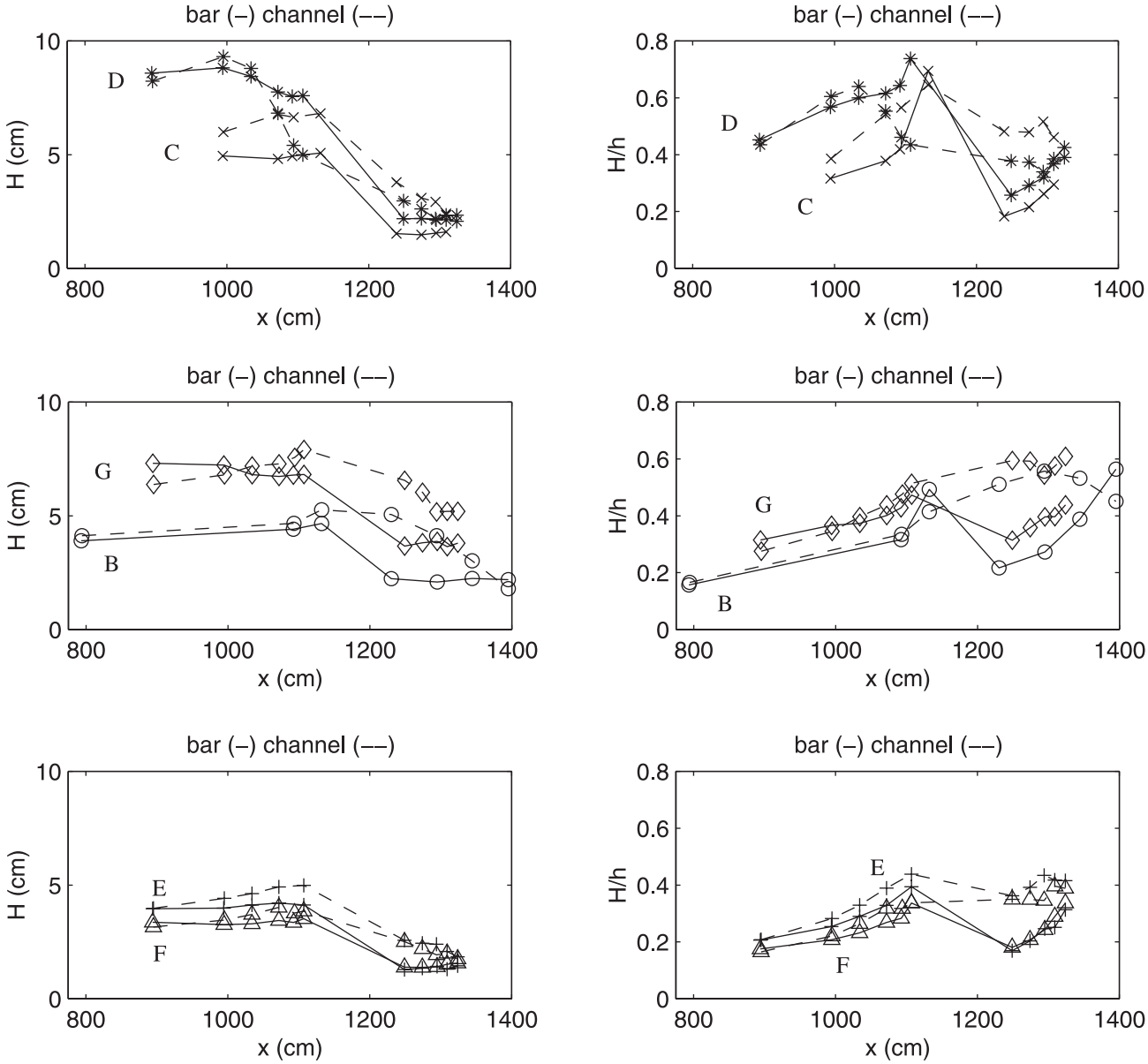

Figure 6. Cross-shore profiles of (left) wave height and (right) H/h. Tests C (crosses) and D (asterisks) represent strong rip current cases, and tests B (circles) and G (diamonds) have weaker rips. Tests E (pluses) and F (triangles) are shown for completeness; h is the total water depth including wave setup.

channels. Thus the presence of the bars and channels induces longshore variation in the cross-shore wave forcing; this generates longshore pressure gradients, which in turn drive feeder currents that converge at the channels and turn offshore as rip currents. The longshore driving forces will be discussed further in section 4.2.

[20] The presence of the rip current and the associated feeder currents is clearly evident in the mean circulation vectors shown in Figures 4d–4f and Figures 5d–5f, and it is apparent that the flow vectors tend to be oriented along the local gradient of the MWL. Figure 5d also indicates that a secondary circulation system exists near the shoreline. This secondary circulation is forced by the breaking of the higher waves that have propagated through the channels. As these waves break close to the shoreline, they drive longshore currents away from the rip channels in the shallowest depths. The spatial extent of this secondary circulation is directly influenced by the degree of high-wave penetration through the rip channel and was visually observed during all of the tests. However, it is only clearly evident in the data from test B because that was the only test in which ADV measurements were obtained close enough to the shoreline. It is important to note that the velocities measured in the rip channel exhibited RMS fluctuations of approximately 5–10 cm/s at timescales of 30–100 s during the tests. These fluctuations have been attributed to a rip current instability [*Haller and Dalrymple*, 2001], but their effects are not considered herein since all data have been averaged over a much longer timescale (~1500 s).

[21] Figure 6 compares cross-shore profiles of H and H/h from transects over the center bar and through the center of the rip channel. It is apparent from Figure 6 (left panels) that with increasing rip strength the waves approaching the rip channel are increasingly steepened relative to those approaching the bar (unless the rip current is not aligned with the wave vector as in test F). The figure also shows that the experiments covered a fairly wide range of offshore wave heights, yet the wave heights measured in the bar trough show less variation from test to test. Comparing the individual tests, wave heights in the trough appear well correlated with the total water depth.

[22] It is known from previous studies that H/h at the onset of breaking is larger for plunging breakers than for spilling breakers [e.g., *Dally et al.*, 1985]. For regular breaking waves in the laboratory, $H/h < 0.78$ is generally the spilling regime, and $H/h > 1.0$ is the plunging regime; however, the influence of currents on H/h at breaking is unclear. Though it seems likely that an opposing rip current will tend to shift spilling breakers toward the plunging regime, therefore H/h at the breakpoint will increase.

[23] Considering the case of a strong rip versus a weak rip as shown in Figure 6 (right panels), it appears that for a weak rip there is little longshore variability in H/h at the breakpoint despite the large difference in the breaking intensity (and breaker type) between the bar and the channel. However, the relatively low measured value of H/h over the bar is partially attributed to the fact that the measuring points are offshore of the bar crest. Indeed, it is likely that the actual values can be approximated by H_{bar}/h_c as listed in Table 1, which are much larger (0.93, test B; 1.01, test G). The value of H/h falls rapidly as the waves enter the bar trough because of the rapid increase in the water depth, but H/h increases again as the waves reshoal and breaking ceases. In contrast, the waves in the channel continue dissipating shoreward of the bars, and H/h remains fairly constant as would be expected from spilling breakers on a constant beach slope.

[24] If we consider H_{bar}/h_c for the strong current case (1.85, test C; 2.83, test D), then H/h shows an even stronger longshore variation at the breakpoint. The measured values of H/h near the bar show an increase from the weak current tests, since the offshore wave heights are larger and the still water depth is lower, and therefore the bar points are closer to the breakpoint, and the high values at the bar crest are better resolved. The values in the channel are also somewhat higher for the strong current case owing to the breaking being closer to plunging. Most importantly, the shoreward evolution of H/h in the channel when the current is very strong (test D) is markedly different from the other tests. This suggests that the nature of the wave dissipation on a spatially varying current is quite different from typical depth-limited breaking. This causes a large longshore variation of H/h, even offshore of the bar where the depth is longshore-uniform.

[25] These results suggest that longshore variable bathymetry and opposing currents significantly influence breaker type (and therefore H/h at the breakpoint) and the shoreward evolution of the breakers. Since, in general, wave breaking is the primary driving mechanism of nearshore circulation (in section 4.2 we will discuss the influence of wave breaking on feeder current strength), this also suggests that significant longshore variability of H/h in the breaking region may need to be accounted for in the modeling of rip current systems.

3.2. Rip Current Flow

[26] Previous observations have made it clear that the existence and relative strength of rip currents are related to the forcing provided by the incident wave field. The influence of water depth variability (due to tides and bathymetry) is slightly less direct, since it is first manifested in the waves, which in turn drive the rips. It is apparent, however, that bathymetry tends to control the location and spacing of the rips and the tidal cycle will modulate the strength of the flow [*Aagaard et al.*, 1997; *Brander*, 1999; *Brander and Short*, 2000]. In our experiments the bathymetry was fixed, but the wave forcing and still water depths were varied. In order to evaluate the relationship between the wave forcing and the rip current strength we compare the following parameters:

$$\begin{aligned} H_r/h_c &\Leftrightarrow U_r', \\ Q_w &\Leftrightarrow Q_r, \end{aligned} \tag{1}$$

where H_r is a representative wave height, h_c is the water depth at the bar crest, U_r' is the mean rip velocity normalized by the linear wave phase speed in the rip channel ($U_r' = U_r/C_{\mathrm{rip}}$), and Q_w is the wave volume flux per unit width given by linear wave theory as

$$Q_w = \frac{1}{8}\frac{gH_r^2}{C_{\mathrm{bar}}}, \tag{2}$$

where g is the gravitational constant and C_{bar} is the wave phase speed near the bar crest. The mean volume flux per unit width in the rip current is given by $Q_r = U_r h_{\mathrm{rip}}$.

[27] Figures 7a and 7b show the relationship between the rip forcing parameters (H_r/h_c, Q_w) and the rip flow parameters (U_r', Q_r). The effects of tides, or in this case the still water level, appear most directly in H_r/h_c. Figure 7a shows an approximately linear relationship between U_r' and H_r/h_c when the wave height just offshore of the bar ($H_r = H_{\mathrm{bar}}$) is used. The case with oblique incidence (test F) appears to deviate strongly from this linear relationship and shows an abnormally strong rip velocity. *Aagaard et al.* [1997] observed a similar effect at small oblique incidence and attributed it to a "wind-enhanced" longshore current. It seems that a more likely explanation is the additional radiation stress forcing in the longshore direction due to the breaking of obliquely incident waves at the bar crest. This additional forcing generates a relatively stronger longshore current behind the center bar (see Figure 18f) and a stronger rip velocity in the downstream channel. An additional influence may be the reduction of the opposing force of the waves on the rip, owing to the slight change in the wave direction. However, it is unclear to what degree the present results are influenced by the downstream sidewall. Model studies suggest that at large incidence angles the feeder currents may have enough inertia to bypass the channel altogether and completely suppress the rip currents [*Svendsen et al.*, 1999].

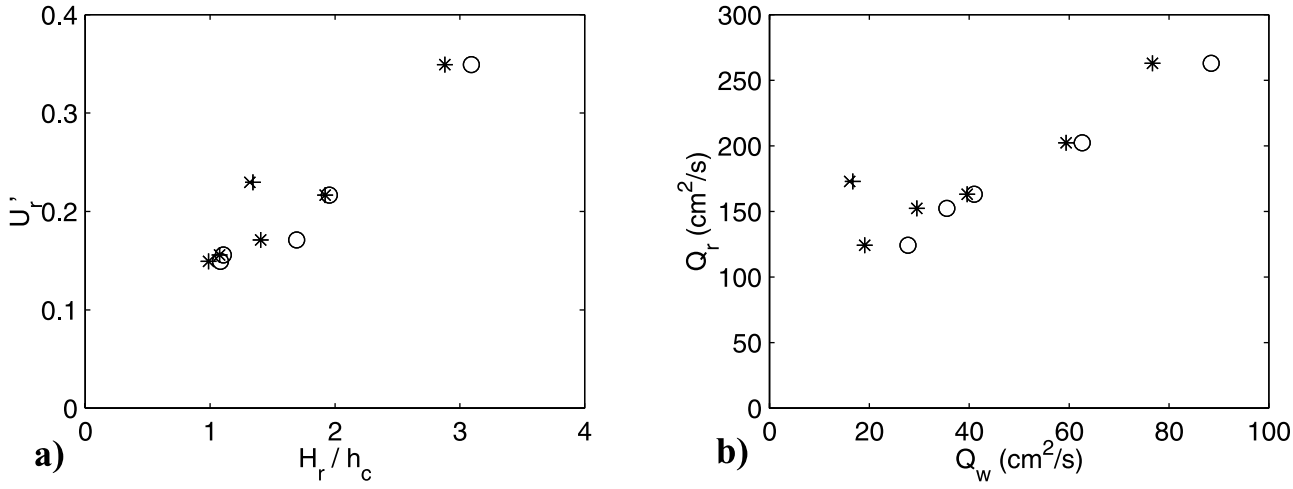

Figure 7. (a) Nondimensional rip velocity versus wave height to water depth ratio determined using $H_r = H_0$ (circles; test F, plus sign) and $H_r = H_{\text{bar}}$ (asterisks; test F, cross) and (b) offshore volume flux in the rip channel versus wave volume flux determined from $H_r = H_0$ (circles; test F, plus sign) and using $H_r = H_{\text{bar}}$ (asterisks; test F, cross).

[28] For comparison, the relationships in equation (2) were examined using the offshore wave height H_0 since this may be an easier parameter to measure in the field. Figure 7a indicates that U_r' also appears to vary linearly with H_0/h_c. However, it is unlikely that either of these linear trends are valid for low values of H_r/h_c since they show nonzero intercepts. The rip flow should tend to zero with the wave height; in fact, it is likely that at some small nonzero value of H_r/h_c the waves would cease breaking at the bar crest and all breaking would occur very near the shoreline. In this scenario the bars would essentially no longer affect the nearshore dynamics, and the rip currents would not be present. Figure 7b compares the volume flux in the rip current with the volume flux of the waves near breaking using both H_{bar} and H_0. For both choices of wave height the offshore rip flux varies linearly with the the wave volume flux. Again, test F shows an increased flux that deviates from the linear trend.

3.3. Depth-Averaged Flow

[29] The present set of velocity measurements were obtained at a single vertical location and do not capture the vertical variability of the nearshore currents. For example, the shoreward wave mass transport is mostly limited to the upper reaches of the water column and is therefore poorly resolved in measurements taken below trough level. Additionally, the presence of a bottom boundary layer will significantly affect the horizontal velocities measured very close to the bottom. Below trough level the cross-shore component of the flow (the undertow) often exhibits strong vertical dependence, especially near the crests of bars [*Garcez Faria et al.*, 2000]. On the other hand, it is usually a reasonable approximation to assume that the longshore component of the flow is depth-uniform in the surf zone.

[30] Since it is difficult to resolve the depth dependence of the cross-shore flows with the measurements, we will calculate the depth-averaged flows by assuming conservation of mass across the measurement grid in order to examine the nearshore momentum balances. The depth- and time-averaged cross-shore and longshore velocities (U and V, respectively) can be related using the continuity equation

$$\frac{\partial}{\partial x}(Uh) + \frac{\partial}{\partial y}(Vh) = 0, \tag{3}$$

where h is the total water depth including wave setup $\overline{\eta}$ and $\partial\overline{\eta}/\partial t$ has been assumed negligible. We will also assume that V is depth-uniform and given by the measurements; therefore we are neglecting the longshore component of the wave mass transport. However, the longshore mass transport is zero everywhere for normally incident waves except for near the rip channel, where some wave refraction and diffraction occurs. Using the measurements of V and h, equation (3) can be integrated to calculate U. The integration requires a boundary condition for U given by the no-flow condition at the shoreline. The integration is stepped in the offshore direction and requires measurements of V reasonably close to the shoreline (further details of the integration are given in Appendix B). These measurements were available shoreward of the center bar for all tests and over an even larger region for test B.

[31] The extensive ADV measurements from test B allow us to calculate the depth- and time-averaged currents throughout the study area as shown in Figure 8. In order to make comparisons between each test simpler, we will nondimensionalize the coordinate system. The cross-shore coordinate is normalized by the distance from the bar crest to the still water shoreline, such that the origin is at the crest and the still water shoreline is at $x' = 1$. The longshore coordinate is normalized by the rip spacing, such that the midpoint of the central bar is at $y' = 0$ and the rip channel centers are located at $y' = \pm 0.5$ (channel extents are $-0.6 < y' < -0.4$ and $0.4 < y' < 0.6$).

[32] The depth-averaged currents in Figure 8 clearly show a circulation pattern consisting of broad regions of

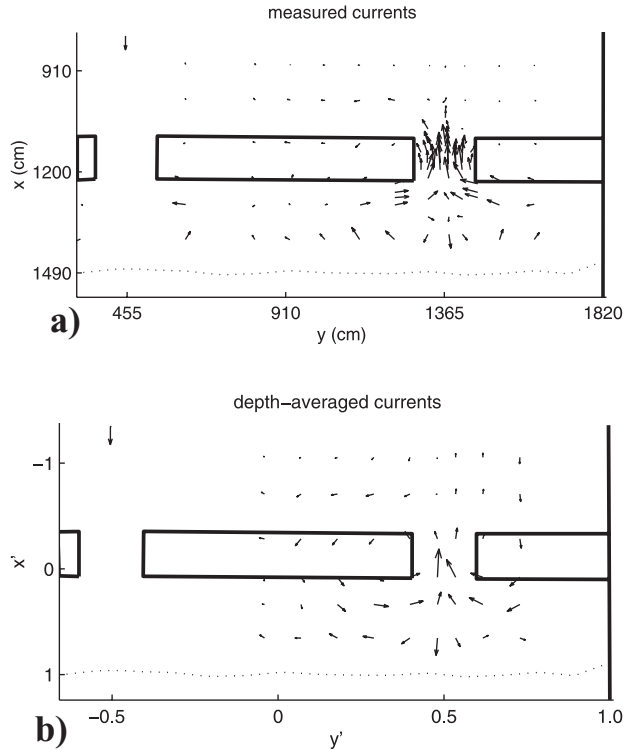

Figure 8. (a) Measured currents, test B, and (b) depth-averaged currents, test B, calculated using equation (3). Vectors at upper left equal 10 cm/s and are shown for scale; MWL is shown as a dotted line.

shoreward flow over the bars on either side of a narrow offshore-directed rip current. It is interesting to note that in the center bar region, relatively far from the rip channel, the depth-averaged cross-shore flow is nonzero. It is commonly assumed that longshore variability can be neglected in regions where the bathymetry is locally longshore-uniform; this assumption would imply that depth-averaged cross-shore currents are zero locally. The presence of nonzero cross-shore flows in the midbar region suggests that the effects of longshore nonuniformity are not localized to the rip channel area.

[33] The influx over the center bar for each test is shown in Figure 9. The data from test B show that shoreward directed flux extends from near the still water shoreline to approximately one surf zone width offshore of the breaker line. The data also indicate that the maximum shoreward flux occurs near the bar crest; tests G and D exhibit the strongest cross-shore flux.

[34] The variation of the cross-shore volume flux along a longshore transect just shoreward of the crest is shown in Figure 10. The figure indicates that the magnitude of the flux over the bar is approximately 20% of the maximum rip flux. The influx is fairly constant, with the maximum occurring near the midpoint between the bar center ($y' = 0$) and the rip channel ($y' = 0.5$). If this rip current exists inside an independent circulation cell, the mean cross-shore flux within $0 < y' < 1$ should be zero. Since the data do not extend all the way to $y' = 1$, in order to do the integration it was first necessary to linearly interpolate the value at $y' = 0$ based on the two nearest data points and then assume that the flux at $y' = 1$ equals the flux at $y' = 0$. The calculated mean flux is -0.14 cm^2/s, which is less than 1% of the mean offshore rip current flux at this cross-shore location. This indicates that the circulation cell is indeed closed. The result is not necessarily surprising, but it is also useful as a check on the procedure for calculating the depth-averaged currents.

4. Nearshore Hydrodynamics

[35] Next, we will examine the nearshore momentum balances using the measured data. In particular, we will compare the cross-shore balance at the center bar with the balance in the rip channel, and we will estimate the important parameters in the driving of the longshore feeder currents and examine the effect of the degree of wave

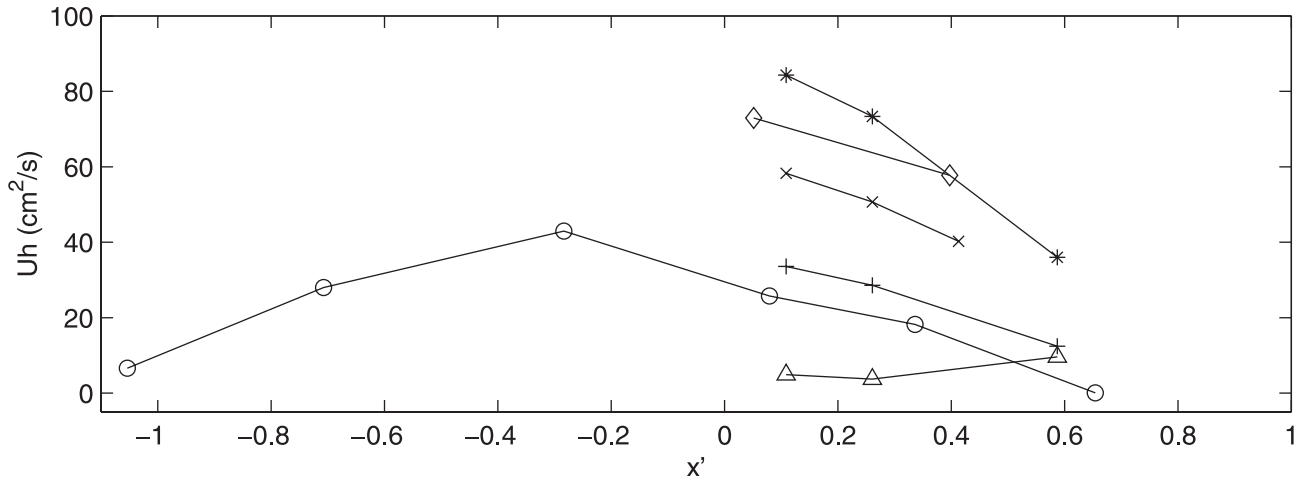

Figure 9. Depth-averaged cross-shore flux over the center bar versus cross-shore distance. Longshore locations are as follows: test E, $y' = 0.12$ (pluses); test C, $y' = 0.12$ (crosses); test D, $y' = 0.12$ (asterisks); test B, $y' = 0.07$ (circles); test G, $y' = 0.12$ (diamonds); and test F, $y' = 0.12$ (triangles).

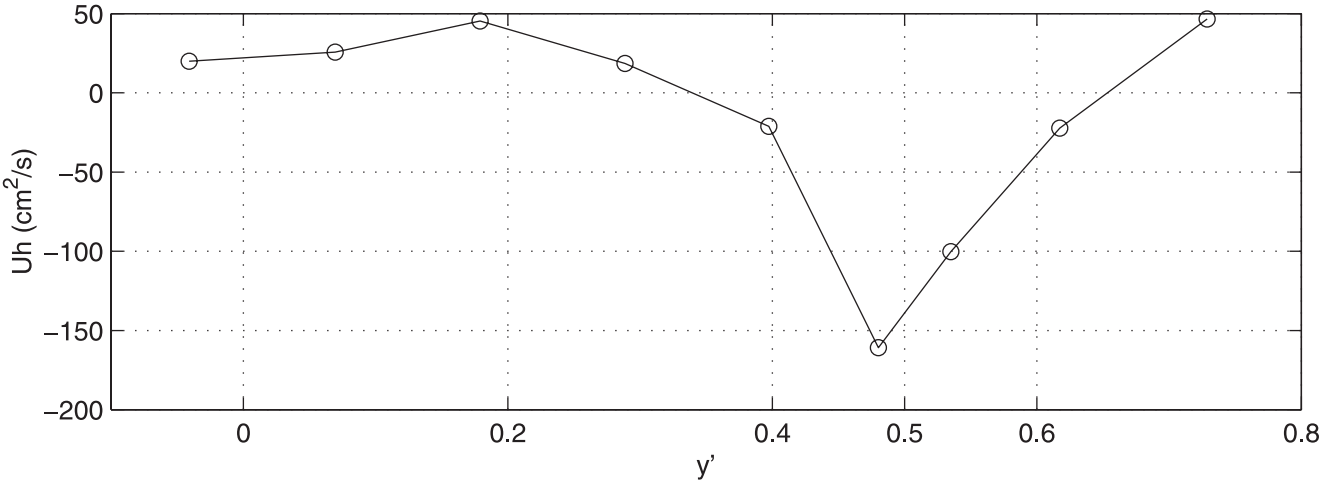

Figure 10. Cross-shore volume flux versus longshore distance, for test B along $x' = 0.08$.

breaking in the rip channel on the driving of the circulation field.

4.1. Cross-shore Momentum Balance

[36] For steady flow the depth- and time-averaged cross-shore momentum equation can be written as

$$\frac{\partial}{\partial x}\left(U^2 h\right) + \frac{\partial}{\partial y}(UVh) = -gh\frac{\partial \overline{\eta}}{\partial x} - \frac{1}{\rho}\left(\frac{\partial S_{xx}}{\partial x} + \frac{\partial S_{yx}}{\partial y}\right) - \frac{\tau_x^b}{\rho}, \quad (4)$$

where ρ is the fluid density, $S_{i,j}$ represents the components of the radiation stress tensor, τ_x^b is the component of bottom stress acting in the x direction, and we have neglected both turbulent mixing and the dispersive mixing caused by the vertical variation of the currents [*Svendsen and Putrevu*, 1994]. The first three terms in equation (4) can be calculated from the depth-averaged currents and the measured surface elevations. The cross-shore radiation stress S_{xx} is given by

$$S_{xx} = \frac{1}{8}\rho g H^2\left[n\left(\cos^2\theta + 1\right) - \frac{1}{2}\right] + \rho g H^2\left(\frac{0.9h}{L}\right), \quad (5)$$

where

$$n = \frac{1}{2}\left[1 + \frac{2kh}{\sinh(2kh)}\right],$$

$k = 2\pi/L$ is given by the linear wave dispersion relation, and θ is the local wave incidence angle. The first term on the right-hand side of equation (5) represents the radiation stress induced by the waves (linear theory), and the second is the radiation stress induced by the presence of the surface roller [*Svendsen*, 1984].

[37] For the remaining terms in equation (4) we assume that $\partial S_{yx}/\partial y$ will be of limited importance since the waves were normally incident for the tests analyzed in this section. This term is likely nonzero in the region very near the rip current owing to current-induced refraction and wave diffraction through the gap in the bar. Nonetheless, it is hoped that this term is small relative to the other terms considered here. In any case, we cannot directly calculate this term or the mixing terms from the present measurements. The bottom stress term is given by

$$\tau_x^b = pc_f\langle|\mathbf{u}|u\rangle, \quad (6)$$

where c_f is an empirical coefficient, $\mathbf{u}$ is the total near-bottom velocity vector, and u is the cross-shore component of the near-bottom velocity vector. It is difficult to specify the coefficient c_f with specific certainty for these experiments as it is likely to have some spatial variability owing to the different bottom roughness of the bars and the beach. *Haas et al.* [1998] estimated a range of $0.005 < c_f < 0.018$ for this experimental basin. Instead of getting bogged down in the details of the friction coefficient we assume a constant value of $c_f = 0.02$, which should represent an upper bound for laboratory-scale currents. For $\mathbf{u}$ and u we will use the measured currents, as opposed to the depth-averaged currents, since they are a better representation of the near-bottom velocity. Note that the calculated bottom stress term includes (as it should) the effects of the orbital current motions, since no filtering has been performed on $\mathbf{u}$.

[38] The extensive wave and current measurements from test B allow us to calculate the value of the terms in equation (4) over a wide area (see Appendix C for the calculation procedure). Figure 11 shows the longshore variation of the flow terms $((\partial/\partial x)(U^2h)$, $(\partial/\partial y)(UVh)$, and $\tau_x^b/\rho)$ at separate cross-shore locations for the region bounded by the seaward edge of the bars and the shoreline. The figure shows that all of the terms are generally small ($O(1\ \mathrm{cm}^2/\mathrm{s}^2)$) except near the rip current. This result is corroborated by the circulation systems shown in Figures 4d–4f and Figures 5d–5f, which indicate that the largest flow magnitudes and strongest flow gradients are found near the rip channel for all tests. The bottom stress is generally much smaller than the nonlinear terms, even in the rip current, although the nonlinear terms are often of opposite sign and will tend to cancel out.

[39] Figure 12 shows the longshore variation of the pressure gradient and radiation stress terms, $gh(\partial\overline{\eta}/\partial x)$

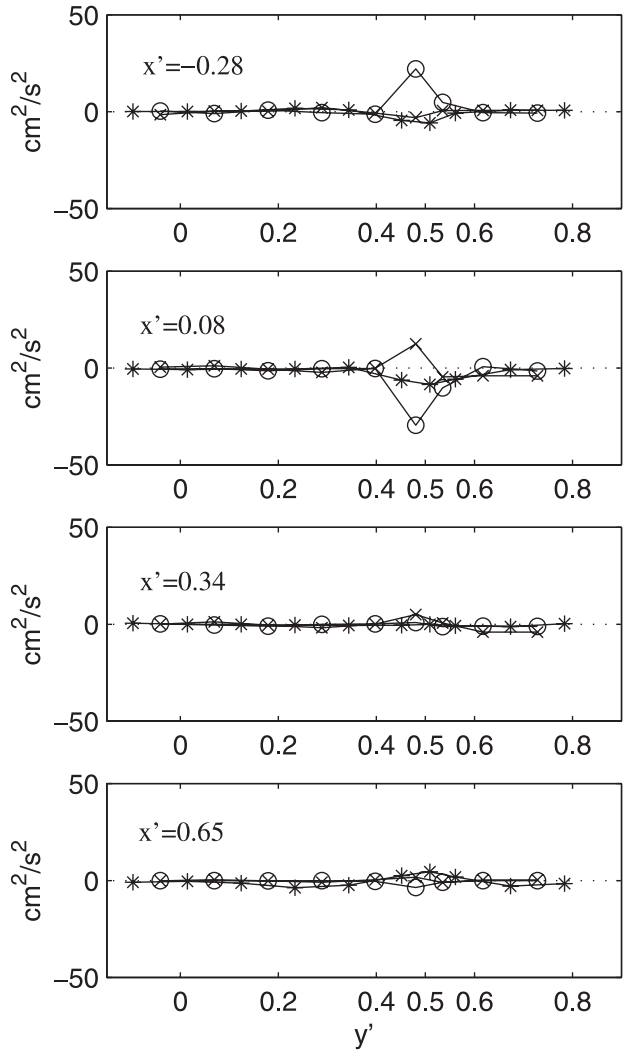

Figure 11. Longshore variation of nonlinear terms $(\partial/\partial x)$ $[U^2h]$ (circles) and $(\partial/\partial y)[UVh]$ (crosses) and bottom stress term τ_x^b/ρ (asterisks) at several cross-shore locations, test B.

and $(\partial/\rho\partial x)S_{xx}$, calculated at similar cross-shore locations as the flow terms. These two momentum terms also show a significant variation based on their proximity to the rip channel. At the offshore line ($x' = -0.23$), $\partial S_{xx}/\partial x$ is weaker in the channel because of the milder breaking on the current as compared to over the bar. However, there is comparatively stronger breaking shoreward of the channel than shoreward of the bars. The pressure gradient term shows a similar variation. At the offshore line it is smaller near the channel than over the bars, and shoreward, the opposite is true. It is evident from Figures 11 and 12 that the pressure gradient and radiation stress terms are generally significantly larger than the nonlinear terms in the areas away from the rip channel, and all four terms are of comparable magnitudes near the channel. This is in agreement with the modeling results of *Haas and Svendsen* [2000].

[40] It is difficult to examine the summation of the individual momentum terms at a given location in order to determine if these terms represent a closed balance. This is because the ADV locations were often somewhat different from the wave gauge locations and, moreover, the nonlinear flow terms are calculated at the midpoints between the longshore locations of the ADVs. Attempts to close the momentum balance using linear interpolations so that all the terms were calculated at the same locations showed significant scatter and were generally unsuccessful. This is likely attributed to the differences in the measuring locations and also the inherent uncertainty in defining c_f. So instead, here we are interested in the general character of the momentum balance and a description of which terms are important in a given location.

[41] The results shown in Figures 11 and 12 suggest that the dominant terms in the cross-shore momentum balance over the bars should be the radiation stress and pressure gradients. Similar conclusions were drawn by *Svendsen and Buhr Hansen* [1986], who modeled the case of normally incident waves and an artificially induced shoreward flow over a longshore uniform bar ($V = S_{xy} = 0$). Their results

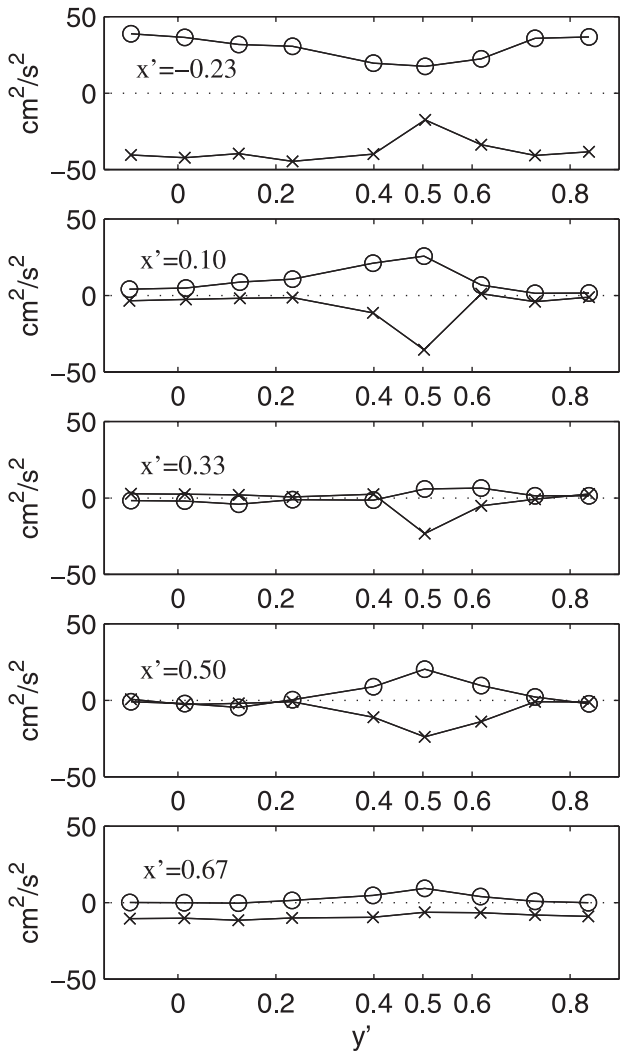

Figure 12. Longshore variation of the pressure gradient $gh(\partial\bar{\eta}/\partial x)$ (circles) and radiation stress forcing $[\partial/(\rho\partial x)]S_{xx}$ (crosses) at several cross-shore locations, test B.

suggested that both the inflow over the bar and the bottom stress had only a limited effect on the wave-induced setup. Instead, the dominant effect of the cross-shore current was to influence the wave height variation, which, in turn, influenced the setup. This suggests that the setup should be governed by

$$\frac{\partial \bar{\eta}}{\partial x} = -\frac{1}{\rho g h}\frac{\partial S_{xx}}{\partial x} \tag{7}$$

as first shown by *Longuet-Higgins and Stewart* [1962]. This balance is tested for the present bar and channel system by comparing the MWL predicted by

$$\bar{\eta}_{i+1} = \bar{\eta}_i - \frac{1}{\rho g h_i}\left(S_{xx_{i+1}} - S_{xx_i}\right), \tag{8}$$

where the radiation stress is calculated from the measured wave heights using equation (5), with the measured MWL along cross-shore transects across the bar and through the channel.

[42] Figures 13–17 compare $\bar{\eta}$ predicted from equation (8) with the measurements. The effect of the roller was included only across (cross-shore) intervals where the waves were actively breaking. This includes the interval spanning $x' = 0$ over the bar and all intervals demonstrating wave decay through the channel. In order to quantify the agreement between the model and measurements we calculate an error function, given by

$$\epsilon = \left[\frac{\sum_{i=1}^{N}\left(\bar{\eta}_{\mathrm{meas}_i} - \bar{\eta}_{\mathrm{pred}_i}\right)^2}{\sum_{i=1}^{N}\bar{\eta}^2_{\mathrm{meas}_i}}\right]^{1/2}, \tag{9}$$

where $\bar{\eta}_{\mathrm{meas}}$ are the measured MWL values and $\bar{\eta}_{\mathrm{pred}}$ are the predicted values. The figures show that the error between $\bar{\eta}_{\mathrm{meas}}$ and $\bar{\eta}_{\mathrm{calc}}$ is generally small over the bar (panel b of Figures 13–17); however, the setup at the shoreline tends to be underpredicted. This is consistent with previous results on longshore uniform barred beaches in the laboratory [*Reniers and Battjes*, 1997] and in the field [*Raubenheimer et al.*, 2001].

[43] The errors between $\bar{\bar{\eta}}_{\mathrm{meas}}$ and $\bar{\eta}_{\mathrm{pred}}$ are typically larger through the channel than over the bar. The maximum setdown and (in contrast to the barred region) the setup at the shoreline tend to be overpredicted owing to the presence of the rip current. Test D shows large differences between $\bar{\eta}_{\mathrm{meas}}$ and $\bar{\eta}_{\mathrm{pred}}$ in the initial breaking region. This is likely due to the presence of very large plunging breakers induced by the rip. It appears that the breaking transition region is much larger in this test, and therefore the increase in $\bar{\eta}_{\mathrm{meas}}$ is shifted shoreward as the wave momentum is first redistributed into the roller before it is dissipated and transferred to $\bar{\eta}_{\mathrm{meas}}$. The total setup at the shoreline, however, is well predicted.

[44] In summary, the details of the cross-shore variation of the MWL near the rip currents are dependent on the current-induced breaking. Since spatial MWL gradients are a driving force of the nearshore circulation, these results suggest that rip current effects on breaker type and location may have a feedback effect on the rip current strength.

4.2. Longshore Momentum Balance

[45] A specific topic of interest involves the role of longshore variability (i.e., rip channels in longshore bars) in the forcing of longshore currents on barred beaches. Field observations on barred beaches under oblique wave attack often show that the strongest longshore current occurs in the trough between the bar and the shoreline [e.g., *Bruun*, 1963; *Greenwood and Sherman*, 1986; *Smith et al.*, 1993]. In contrast to the measurements, longshore current models that assume longshore uniformity tend to predict longshore velocity profiles with maxima near the bar crest. Early studies [*Bowen*, 1969; *Mei and Liu*, 1977; *Dalrymple*, 1978] had suggested that longshore variability could play a significant role in the distribution of nearshore currents. Recent numerical model studies [*Putrevu et al.*, 1995; *Reniers et al.*, 1995; *Sancho et al.*, 1995; *Slinn et al.*, 2000] have analyzed the importance of longshore pressure gradients on the longshore current, and the combined efforts demonstrate that small longshore pressure gradients can drive strong longshore currents, especially when wave incident angles are small.

[46] Figures 4d–4f and Figures 5d–5f suggest that much of the nearshore circulation on this bar-channel topography is being driven by MWL gradients. For normally incident waves the longshore pressure gradient is the only available driving force for the generation of the longshore feeder currents that converge at the base of the rip current. Figure 18 shows the cross-shore profiles of the feeder currents shoreward of the center bar for each test. The feeder currents ramp up from near zero at $y' = 0$ to their maxima near $y' = 0.30$–0.34. At locations even closer to the rip channel the longshore flow decreases. Also, the data show that the current maxima were of similar magnitude for most of the tests; test D exhibits the strongest feeder currents and rip currents and the highest waves.

[47] The cross-shore locations of the current maxima are generally between $x' = 0.25$ and $x' = 0.45$, which is significantly shoreward of the bar crest. This clearly demonstrates that longshore feeder currents, induced by the periodic depressions in a longshore bar, have maxima shoreward of the bar crest. The data from test F, with mildly oblique wave incidence, show two relatively large current maxima, one in the trough and one near the bar crest. The second maximum is driven by the oblique wave breaking at the bar crest, and this increased longshore flow had the added effect of causing the rip current to exit the channel at a significantly oblique angle (see Figure 5f). These data provide strong experimental evidence that longshore bathymetric variability can play a significant role in the nature of longshore current profiles on barred beaches and can shift the longshore current maximum shoreward of the bar crest. However, it should be noted that it is still unclear how longshore current maxima will be affected in regions where pressure-driven (feeder) currents flow against the wave direction.

[48] The depth- and time-averaged longshore momentum equation can be written as

$$\frac{\partial}{\partial x}(UVh) + \frac{\partial}{\partial y}\left(V^2 h\right) = -gh\frac{\partial \bar{\eta}}{\partial y} - \frac{1}{\rho}\left(\frac{\partial S_{yy}}{\partial y} + \frac{\partial S_{xy}}{\partial y}\right) - \frac{\tau_y^b}{\rho}, \tag{10}$$

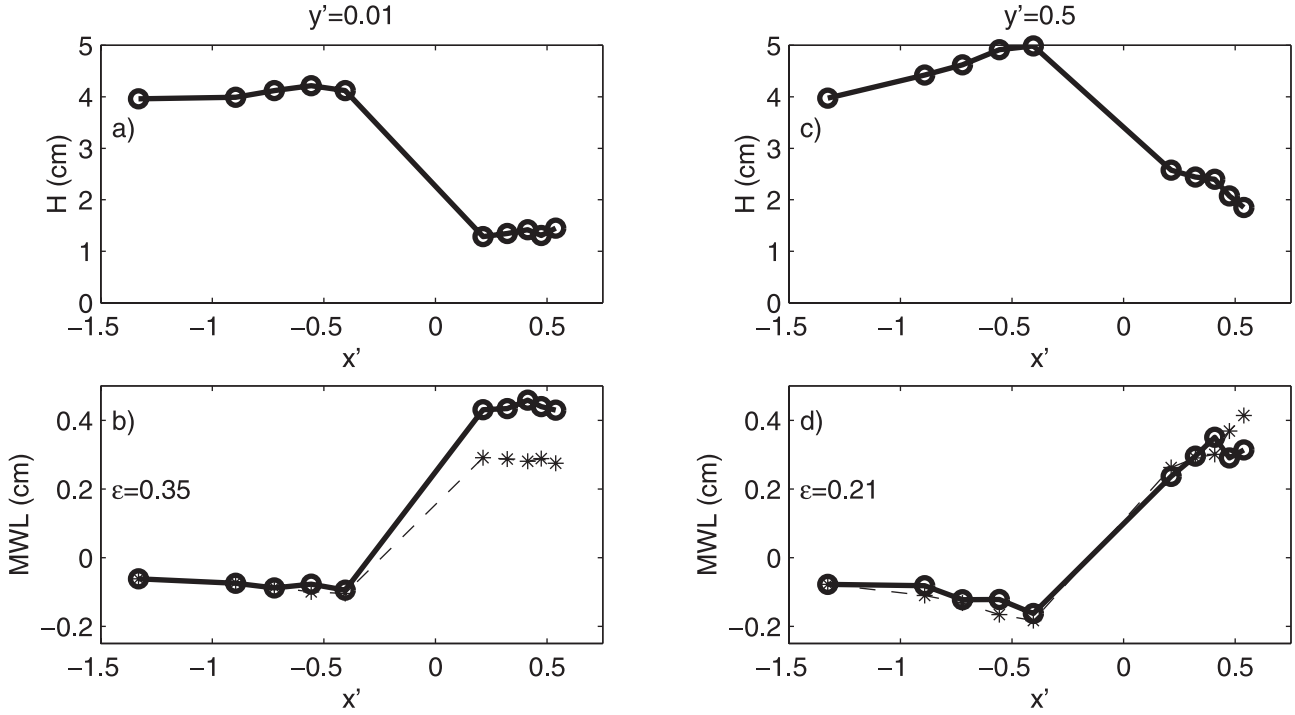

Figure 13. Wave height and MWL versus cross-shore distance (a and b) at the center bar and (c and d) at the rip channel, for test E. Measured values, circles; calculated MWL from radiation stress gradients, asterisks.

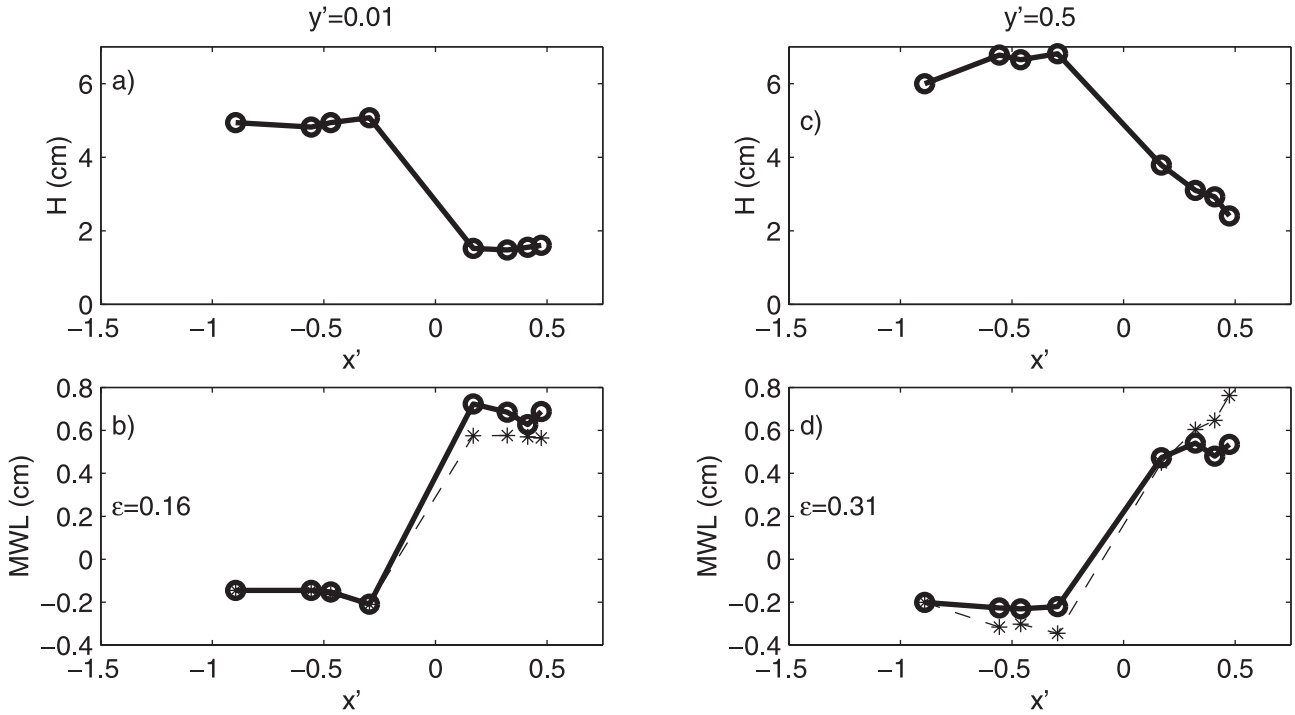

Figure 14. Wave height and MWL versus cross-shore distance (a and b) at the center bar and (c and d) at the rip channel, for test C. Measured values, circles; calculated MWL from radiation stress gradients, asterisks.

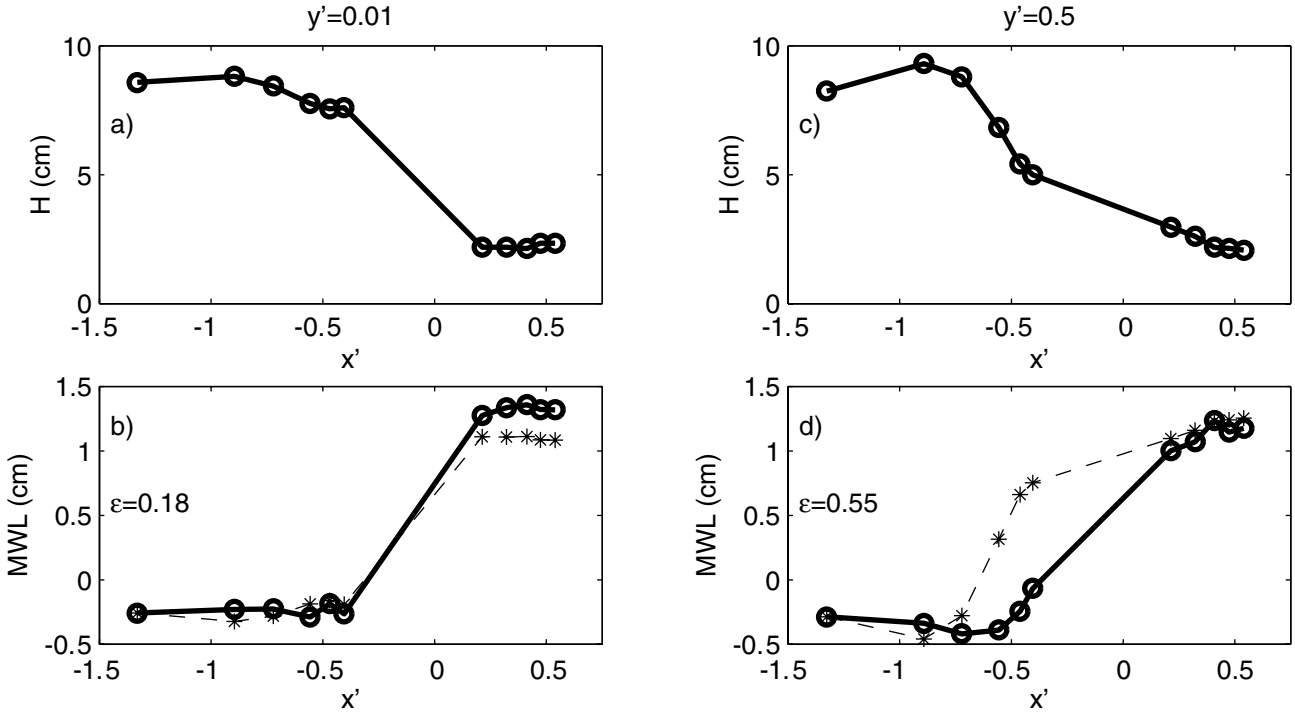

Figure 15. Wave height and MWL versus cross-shore distance (a and b) at the center bar and (c and d) at the rip channel, for test D. Measured values, circles; calculated MWL from radiation stress gradients, asterisks.

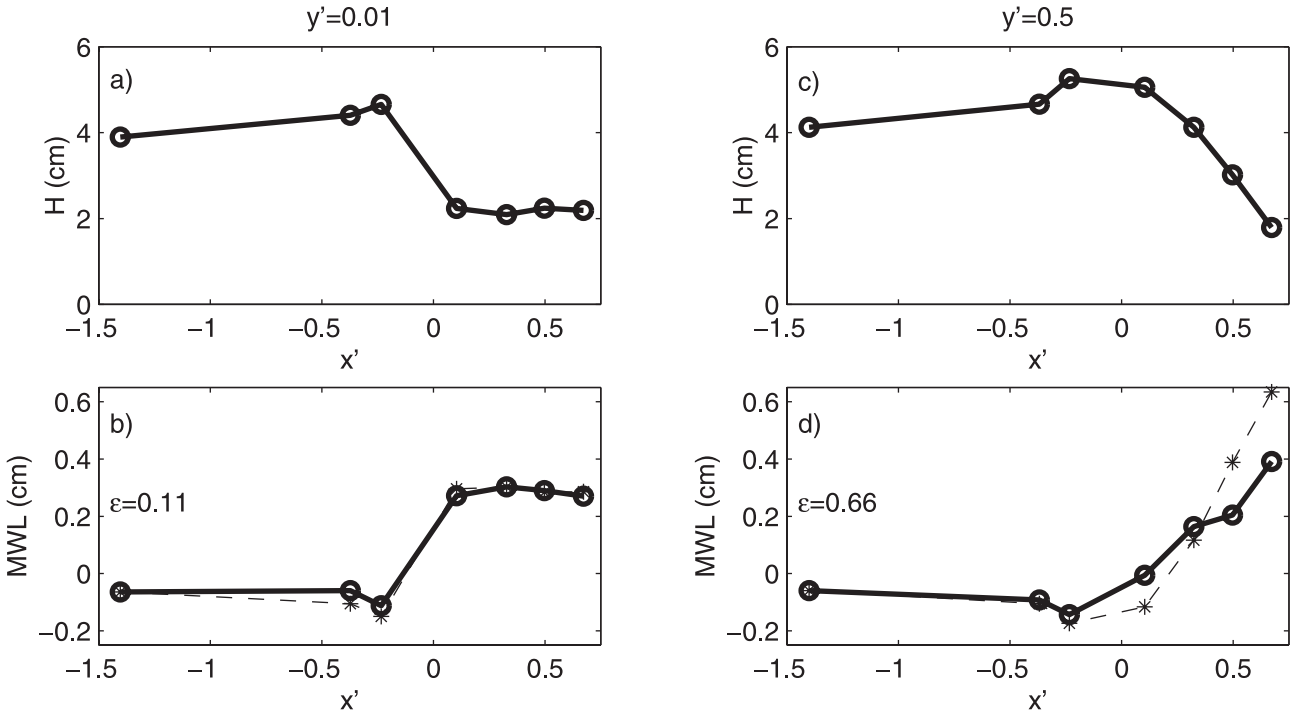

Figure 16. Wave height and MWL versus cross-shore distance (a and b) at the center bar and (c and d) at the rip channel, for test B. Measured values, circles; calculated MWL from radiation stress gradients, asterisks.

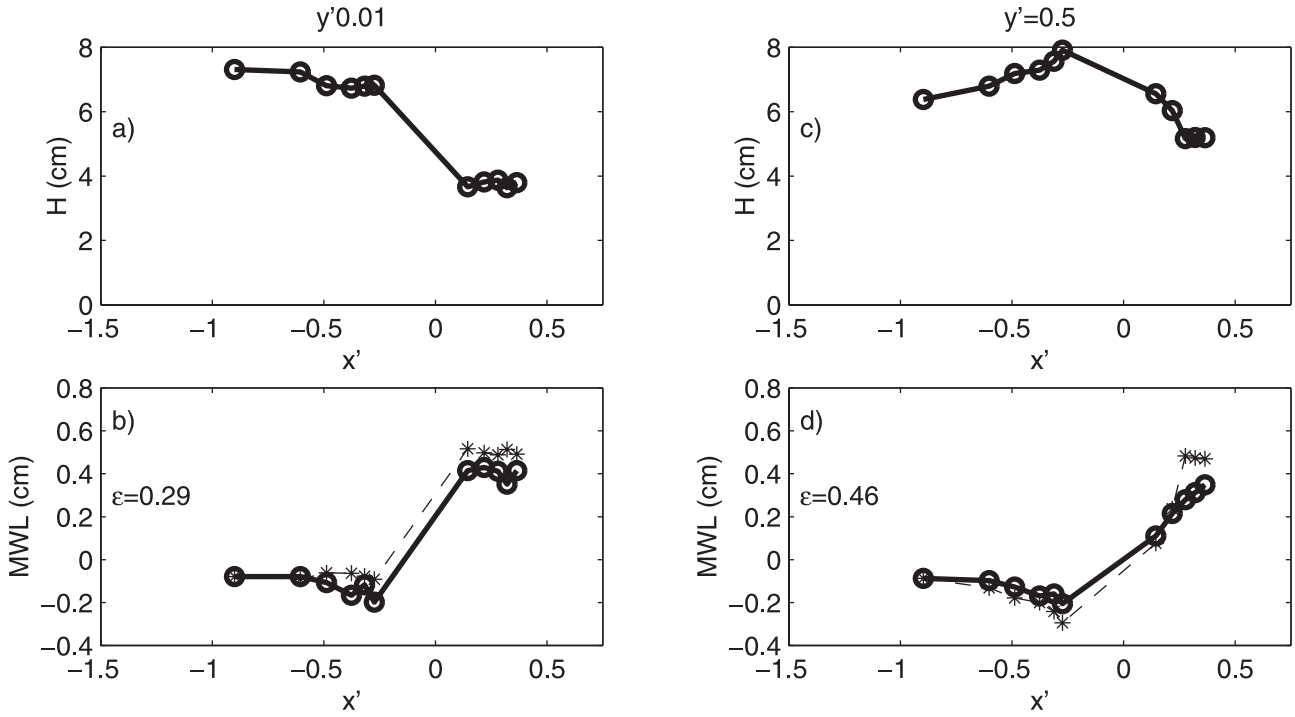

Figure 17. Wave height and MWL versus cross-shore distance (a and b) at the center bar and (c and d) at the rip channel, test G. Measured values, circles; calculated MWL from radiation stress gradients, asterisks.

where, for normally incident waves, the longshore radiation stress component is given by

$$S_{yy} = \frac{1}{8}\rho g H^2 \left[n - \frac{1}{2} \right], \tag{11}$$

S_{xy} is again neglected, and τ_y^b is the component of the bottom stress acting in the y direction given by

$$\tau_y^b = 0.02\rho \langle |\mathbf{u}| v \rangle. \tag{12}$$

Figure 19a shows the amplitude of the longshore pressure gradient forcing just shoreward of the bar crest. Initially, one might expect that feeder current strength would scale with the pressure gradient. However, it appears that this is not entirely true. The pressure gradients in the region shoreward of the center bar are generally similar for all the tests, but tests B and G show the largest gradients. This is somewhat puzzling since their feeder currents are not nearly as strong as those of test D.

[49] Some insight is gained by looking at the wave height contours shown in Figures 4a–4c and Figures 5a–5c and the opposing radiation stress forcing shown in Figure 19b. The wave height contours show that, while wave breaking occurred in the channel for all tests, at higher water levels (tests B and G), high waves penetrate farther shoreward past the bars. The degree of high-wave penetration through the rip channel governs the longshore wave height variation shoreward of the bars and will influence the longshore forcing of currents in this region. Tests B and G show an increased level of opposing radiation stress forcing shore-

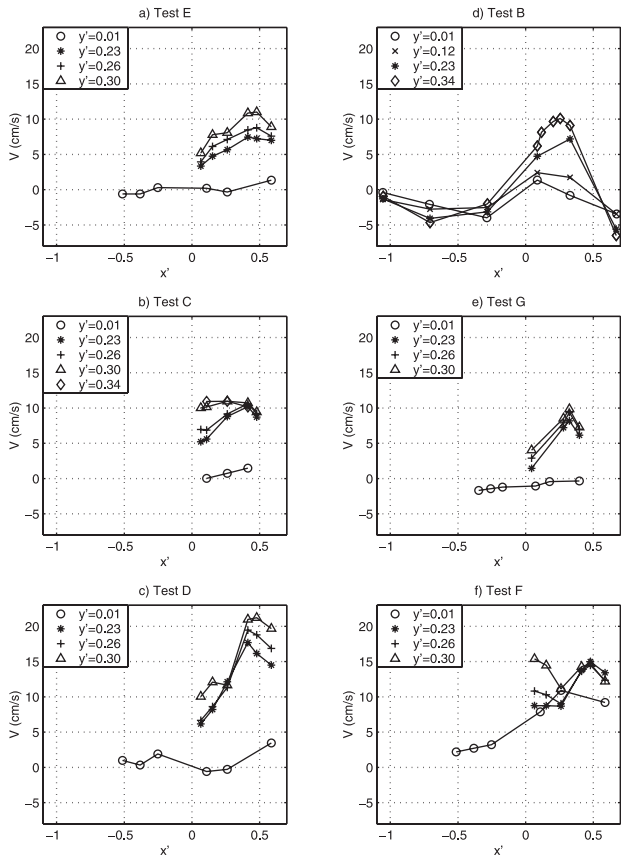

Figure 18. Cross-shore profiles of measured longshore current for (a) test E, (b) test C, (c) test D, (d) test B, (e) test G, and (f) test F.

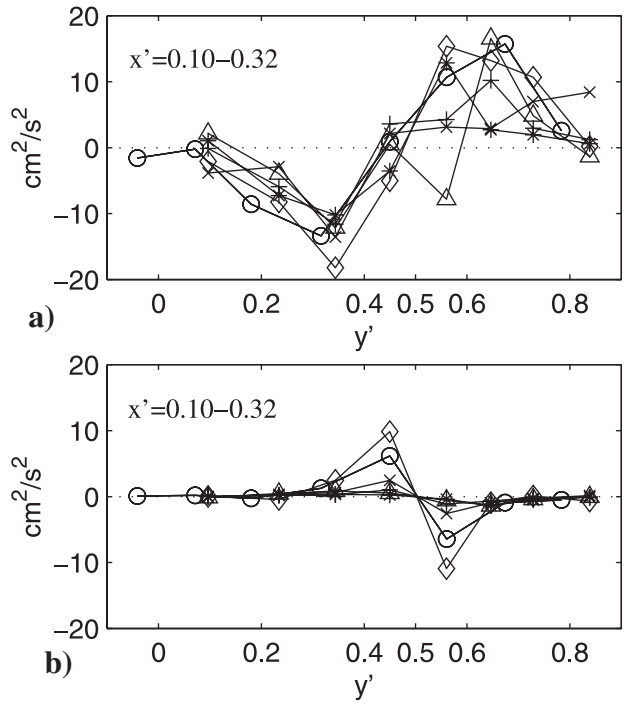

Figure 19. (a) Longshore pressure gradient $gh(\partial\bar{\eta}/\partial y)$ and (b) radiation stress gradient $[\partial/(\rho\partial y)]S_{yy}$ versus longshore distance shoreward of the bar crest for test E, $x' = 0.21$ (pluses); test C, $x' = 0.17$ (crosses); test D, $x' = 0.32$ (asterisks); test B, $x' = 0.10$ (circles); test G, $x' = 0.14$ (diamonds); and test F, $x' = 0.21$ (triangles).

ward of the bar crest, which may explain why these tests do not show an increased feeder strength. Additionally, test D has essentially zero radiation stress gradient available to oppose the feeder current.

[50] The gradients measured even closer to the shoreline (Figure 20) offer further insight. The pressure gradient reverses sign close to the rip for tests B and G, and this positive pressure gradient drives the secondary circulation that flows away from the channels close to shore. For test G the sign reversal of the pressure gradient occurs farther from the shoreline. In fact, the positive pressure gradient extends over more than half of the surf zone width. Test G also shows the largest radiation stress gradient driving flow away from the channel at the most shoreward measuring location; therefore test G has the largest secondary circulation. The increased secondary circulations in test B and G also imply that the feeder currents are reduced in width with respect to x', as can be seen in Figures 18d and 18e. In general, the secondary circulation must also exert a shear stress on the feeder currents and is likely an additional factor limiting the feeder current strength.

[51] In order to simplify the analysis of the longshore driving forces, let us integrate equation (10) from the midpoint between rips ($y' = 0$) to the rip centerline ($y' = 0.5$), which gives the following:

$$I_1(x') + I_2(x') = -I_3(x') - I_4(x') - I_5(x'), \qquad (13)$$

where

$$I_1(x') = \int_{y'=0}^{y'=0.5} \frac{\partial}{\partial x}(UVh)dy',$$

$$I_2(x') = \int_{y'=0}^{y'=0.5} \frac{\partial}{\partial y}(V^2h)dy',$$

$$I_3(x') = \int_{y'=0}^{y'=0.5} gh\frac{\partial\bar{\eta}}{\partial y}dy',$$

$$I_4(x') = \int_{y'=0}^{y'=0.5} \frac{1}{\rho}\frac{\partial Syy}{\partial y}dy',$$

$$I_5(x') = \int_{y'=0}^{y'=0.5} \frac{1}{\rho}\tau_y^b dy'.$$

The details of this integration are given in Appendix C. Figure 21 shows the cross-shore profiles of the nonlinear terms ($I_1 + I_2$), the net forcing ($I_3 + I_4$), and the bottom stress ($-I_5$) for test B. It is only possible to examine the variation of these sets of terms, as opposed to calculating the complete balance, since they are not all calculated at the same locations. Also, there remains the inherent uncertainty in the bottom friction coefficient.

[52] Comparison with Figure 18d shows that the bottom stress profile is quite similar to the longshore current profile. According to the balance given by equation (13), $I_1 + I_2 + I_3 + I_4 = -I_5$; however, it appears that this balance may not be complete. For example, it is clear that the net forcing has a maximum near the bar crest while the current maximum is

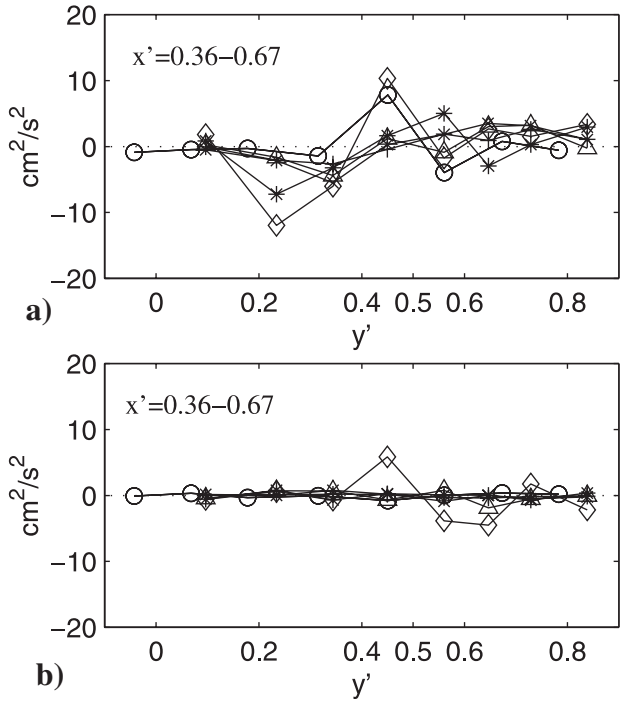

Figure 20. (a) Longshore pressure gradient $gh(\partial\bar{\eta}/\partial y)$ and (b) radiation stress gradient $[\partial/(\rho\partial y)]S_{yy}$ versus longshore distance close to the shoreline for test E, $x' = 0.54$ (pluses); test C, $x' = 0.47$ (crosses); test D, $x' = 0.54$ (asterisks); test B, $x' = 0.67$ (circles); test G, $x' = 0.36$ (diamonds); and test F, $y' = 0.21$ (triangles).

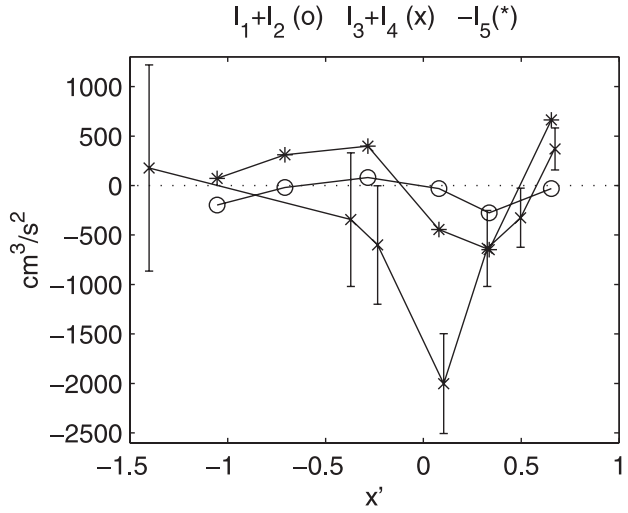

Figure 21. Cross-shore profiles of longshore momentum terms integrated from $y' = 0$ to $y' = 0.5$ and calculated using data from test B. Error bars are based on measurement uncertainties given in section 2.3.

more shoreward. This implies that something other than direct forcing is shifting the current maximum further into the trough. The profile of the nonlinear terms suggests that they may play a role in shifting the current maximum shoreward from the bar crest.

[53] The influence on the strength of the feeder currents of the opposing radiation stress and pressure gradients near the channel, and the associated secondary circulation, suggests that there may be a feedback mechanism between the rip current and the forcing of the feeder currents. For example, in test G there is only limited breaking in the channel; therefore the relatively higher waves that survive through the gap in the bar generate radiation stress gradients, pressure gradients, and a secondary circulation that act to oppose the feeder current and therefore reduce the flows in the feeder and in the rip. In contrast, in test D the waves break much farther offshore, and higher waves do not survive through the gap. Therefore there is no opposing radiation stress in the surf zone. This allows a stronger feeder current and a stronger rip. An ad hoc comparison is made in Figure 22, which shows the cross-shore mean ($0 < x' < 0.5$) of $I_3 + I_4$ versus the mean rip velocity. The data show that there exists a correlation between the net forcing in the feeder region and the rip velocity. Again, test F shows an abnormally large rip velocity because the forcing due to the nonzero S_{xy} has not been accounted for here.

5. Summary

[54] Data from a set of laboratory experiments on a bar-channel topography show that the nearshore dynamics are dominated by the presence of the bars and rip channels on this experimental beach. Contours of wave height demonstrate that the longshore variability of the bathymetry and the current field significantly affects the nature and location of wave breaking. The contrast in wave evolution through the rip channels and over the bars induces a relative increase of the water level in the bar trough region and causes the MWL to slope downward toward the rip channels. The associated longshore pressure gradients drive feeder currents that converge at the channels and turn offshore as rip currents.

[55] Utilizing the conservation of mass principle, the depth-averaged current fields are calculated for the measurement grid. The inflow over the bar, which supplies much of the rip current flow, is shown to span almost the entire length of the longshore bars. The terms in both the cross-shore and longshore momentum balances are calculated, and their relative magnitudes are quantified. The longshore feeder currents exhibit maxima in the bar trough region, providing experimental evidence that longshore pressure gradients can shift longshore current maxima shoreward from the bar crest. The balances in both directions are shown to be dominated by gradients in pressure and radiation stress; however, the nearshore dynamics are also affected by the influence of the opposing rip current on the wave dissipation in the rip channel.

[56] The longshore variations in the bathymetry and the strong rip currents significantly influence breaker type and the wave height to water depth ratio at the breakpoint. The generally reduced wave dissipation through the rip channel means that wave heights can be higher near the channel and generate a longshore radiation stress gradient that opposes the feeder currents. Also, as the waves in the channel break at the shoreline there is an increase in the local wave setup that drives a secondary circulation away from the channels. When the secondary circulation is sufficiently strong, it must also exert an opposing shear stress on the feeder currents. Alternatively, when the rip current is sufficiently strong, the waves in the channel are highly dissipated by current-induced breaking effects and the secondary circulation and the forces opposing the feeder currents are significantly reduced. This suggests that a feedback mechanism may exist whereby a strong rip current can weaken the radiation stress gradients opposing the feeder currents and lead to even stronger feeder currents and rips. Therefore the details of wave

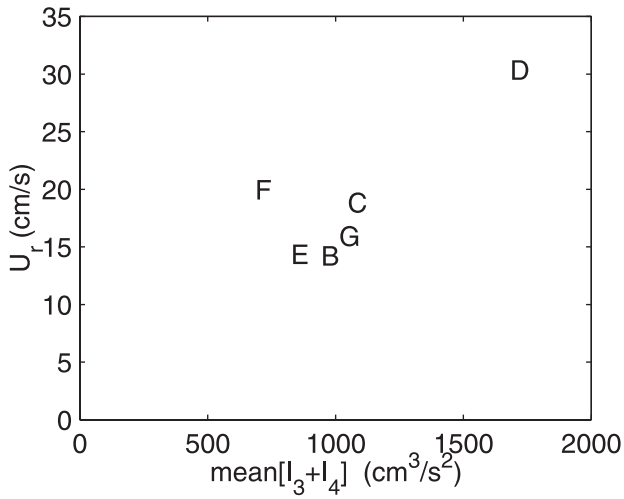

Figure 22. Rip current velocity versus mean forcing within $0 < x' < 0.5$ for each test.

breaking on the opposing rip current should be considered in future modeling efforts.

Appendix A: Error Estimation

[57] Three sources for variability in the time average (over some time interval) of H and η have been identified. First, near the rip current these quantities may vary on timescales of 30–100 s because of the presence of rip instabilities. Second, the time average of η is calculated relative to the average of two still water zero measurements made before and after a given experimental run. This reference zero showed some drift over the 30 min required per run. Third, there is some systematic error in the experimental system that prevents the hydrodynamic conditions from being exactly repeatable from run to run. This error is related to the mechanical wave generating system and to the complex turbulent nature of the rip flow.

[58] In order to quantify the repeatability of the time-averaged quantities, where repeated measurements at a given spatial location exist, the data were divided into n bins of 1024 points (102.4 s) and the set of time-averaged quantities $\bar{H}_i$, and $\bar{\eta}_i$ (i = 1 to n) were calculated. Since the first source of error is a periodic fluctuation in the mean, it should be removed by the binning process. The standard deviation of the means σ_m is then given by the relationship

$$\sigma_m = \frac{\sigma}{\sqrt{n}}, \tag{A1}$$

where σ is the standard deviation of the n estimates of the mean [*Beckwith and Buck*, 1969]. On the basis of this analysis we find that the first source of error is well removed by the binning process, the second source of error is relatively minor, and the third source is the most significant. Additionally, the third source of error is larger in the surf zone and near the rip channels, although it should be noted that only a limited set of measurements were repeated in the surf zone and, therefore, the error estimates are increased because of statistical uncertainty (i.e., n is small). The upper bounds on the repeatability estimates are ±4% for $\bar{H}$ and ±0.02 cm for $\bar{\eta}$.

Appendix B: Continuity Integration

[59] The continuity equation (3) can be written in finite difference form as

$$\frac{(Uh)_{i+1,j+(1/2)} - (Uh)_{i,j+(1/2)}}{x_{i+1,j+(1/2)} - x_{i,j+(1/2)}} = -\frac{(Vh)_{i,j+1} - (Vh)_{i,j}}{y_{i,j+1} - y_{i,j}}, \tag{B1}$$

where i and j are the x and y indices, respectively, and $V_{i,j}$ is given directly by the ADV measurements. The total water depth $h_{i,j}$ is estimated by linearly interpolating h to the ADV measuring locations using the measurements at each wave gauge ($h_{k,l}$). To solve this equation for $(Uh)_{i,j+(1/2)}$ requires a boundary condition for Uh at the mean water line $x_{\mathrm{mwl},j+(1/2)}$. It is natural to impose $Uh = 0$ at the mean water line; the difficulty is determining $x_{\mathrm{mwl},j+(1/2)}$.

[60] Given a set of wave gauge measurements, $\bar{\eta}_{i,j}$ and $h_{i,j}$, along a cross-shore line in the surf zone, the mean water line can be estimated from the following two equations (if, e.g., i = 1, 2, 3):

$$\bar{\eta}_{\mathrm{mwl}} = (x_{\mathrm{mwl}} - x_{\mathrm{swl}})\alpha, \tag{B2}$$

$$\bar{\eta}_{\mathrm{mwl}} = \left(\frac{\partial\bar{\eta}}{\partial x}\right)_s (x_{\mathrm{mwl}} - x_3) + \overline{\eta_3}, \tag{B3}$$

where $\bar{\eta}_{\mathrm{mwl}}$ is the setup at x_{mwl}, α is the local beach slope (α = 1/26.8), $(\partial\bar{\eta}/\partial x)$ is the mean surf zone water surface slope $((\bar{\eta} - \bar{\eta})/(x_3 - x_1))$, and $x3$ is the wave measuring point closest to the shoreline. Equation (B2) states that the total water depth is zero at x_{mwl}, and equation (B3) estimates the setup at x_{mwl} by extrapolating the measured surf zone water surface slope to the mean water line. These two equations are combined and solved for x_{mwl}, and then equation (B1) can be solved for $(Uh)_{i,j+(1/2)}$ and marched offshore. The calculated depth-averaged currents are then $U_{i,j+(1/2)}$, $V_{i,j+(1/2)}$ where $V_{i,j+(1/2)} = (V_{i,j}+V_{i,j+1})/2$. Note that for equation (B1) the scheme for the cross-shore derivative is $O(\Delta x)$, and the longshore derivative is $O(\Delta y^2)$.

Appendix C: Momentum Term Calculations

[61] The terms in equation (4) can be calculated by

$$\left.\frac{\partial}{\partial x}(U^2h)\right|_{i,j+(1/2)} = \frac{(U^2h)_{i+1,j+(1/2)} - (U^2h)_{i,j+(1/2)}}{x_{i+1,j+(1/2)} - x_{i,j+(1/2)}} + O(\Delta x), \tag{C1}$$

$$\left.\frac{\partial}{\partial y}(UVh)\right|_{i,j+(1/2)} = \frac{(UVh)_{i,j+(3/2)} - (UVh)_{i,j+(1/2)}}{y_{i+1,j+(3/2)} - y_{i,j+(1/2)}} + O(\Delta y), \tag{C2}$$

$$\left.-gh\frac{\partial\bar{\eta}}{\partial x}\right|_{k,l} = -gh_{k,l}\frac{\bar{\eta}_{k+1,l} - \bar{\eta}_{k,l}}{x_{k+1,l} - x_{k,l}} + O(\Delta x), \tag{C3}$$

$$\left.-\frac{1}{\rho}\frac{\partial S_{xx}}{\partial x}\right|_{k,l} = -\frac{1}{\rho}\frac{S_{xx_{k+1,l}} - S_{xx_{k,l}}}{x_{k+1,l} - x_{k,l}} + O(\Delta x), \tag{C4}$$

where $S_{xx} = 0$ has been assumed at $x = x_{\mathrm{mwl}}$. The first term in equation (10) can be written as

$$\frac{\partial}{\partial x}(UVh) = V\frac{\partial}{\partial x}(Uh) + Uh\frac{\partial}{\partial x}V = -V\frac{\partial}{\partial y}(Vh) + Uh\frac{\partial}{\partial x}V,$$

and therefore the terms are given by

$$\left.\frac{\partial}{\partial x}(UVh)\right|_{i,j+(1/2)} = -V_{i,j+(1/2)}\left(\frac{(Vh)_{i,j+1} - (Vh)_{i,j}}{y_{i+1,j+1} - y_{i,j}}\right) + (Uh)_{i,j+(1/2)}\left(\frac{V_{i+1,j+(1/2)} - V_{i,j+(1/2)}}{x_{i+1,j+(1/2)} - x_{i,j+(1/2)}}\right) + O(\Delta x) + O(\Delta y^2), \tag{C5}$$

$$\left.\frac{\partial}{\partial y}(V^2h)\right|_{i,j+(1/2)} = \frac{(V^2h)_{i,j+1} - (V^2h)_{i,j}}{y_{i,j+1} - y_{i,j}} + O(\Delta y^2), \tag{C6}$$

$$\left.-gh\frac{\partial\bar{\eta}}{\partial y}\right|_{k,l+(1/2)} = -gh_{k,l+(1/2)}\frac{\bar{\eta}_{k,l+1} - \bar{\eta}_{k,l}}{y_{k,l+1} - y_{k,l}} + O(\Delta y^2), \tag{C7}$$

$$-\frac{1}{\rho}\frac{\partial S_{yy}}{\partial y}\bigg|_{k,l+(1/2)} = -\frac{1}{\rho}\frac{S_{yy_k,l+1} - S_{yy_k,l}}{y_{k,l+1} - y_{k,l}} + O(\Delta y^2). \quad \text{(C8)}$$

The integration of most of the terms in equation (13) can be carried out fairly directly. For example,

$$I_2(x') = \left(V^2 h\right)\Big|_{y'=0}^{y'=0.5}, \quad \text{(C9)}$$

$$I_3(x') = \int_{y'=0}^{y'=0.5} g(h_0 + \bar{\eta})\frac{\partial \bar{\eta}}{\partial y}dy' = g\left(\frac{\bar{\eta}^2}{2} + h_0\bar{\eta}\right)\Big|_{y'=0}^{y'=0.5}, \quad \text{(C10)}$$

$$I_4(x') = \frac{1}{\rho}S_{yy}\Big|_{y'=0}^{y'=0.5}. \quad \text{(C11)}$$

The integrals I_1 and I_5 are integrated using the trapezoidal rule applied to the set of longshore points.

[62] **Acknowledgments.** Funding for this research was provided by the Office of Naval Research Coastal Dynamics Program under grants N00014-95-1-0075 and N00014-98-1-0521, and by the University of Michigan. M. C. Haller would like to thank Rob Holman and H. Tuba Özkan-Haller for their constructive comments on the manuscript and Francisco Sancho and Michael Davidson for their help during the experiments.

References

Aagaard, T., B. Greenwood, and J. Nielsen, Mean currents and sediment transport in a rip channel, *Mar. Geol.*, *140*, 25–45, 1997.

Beckwith, T. G., and N. L. Buck, *Mechanical Measurements*, Addison-Wesley-Longman, Reading, Mass., 1969.

Bowen, A. J., Rip currents, 1, Theoretical investigations, *J. Geophys. Res.*, *74*, 5467–5478, 1969.

Bowen, A. J., and D. L. Inman, Rip currents, 2, Laboratory and field observations, *J. Geophys. Res.*, *74*, 5479–5490, 1969.

Bowman, D., D. Arad, D. S. Rosen, E. Kit, R. Goldbery, and A. Slavicz, Flow characteristics along the rip current system under low-energy conditions, *Mar. Geol.*, *82*, 149–167, 1988a.

Bowman, D., D. S. Rosen, E. Kit, D. Arad, and A. Slavicz, Flow characteristics at the rip current neck under low-energy conditions, *Mar. Geol.*, *79*, 41–54, 1988b.

Brander, R. W., Field observations on the morphodynamic evolution of a low-energy rip current system, *Mar. Geol.*, *157*, 199–217, 1999.

Brander, R. W., and A. D. Short, Morphodynamics of a large-scale rip current system at Muriwai Beach, New Zealand, *Mar. Geol.*, *165*, 27–39, 2000.

Bruun, P., Longshore currents and longshore troughs, *J. Geophys. Res.*, *68*, 1065–1078, 1963.

Cooke, D. O., The occurrence and geologic work of rip currents off southern California, *Mar. Geol.*, *9*, 173–186, 1970.

Dally, W. R., R. G. Dean, and R. A. Dalrymple, Wave height variation across beaches of arbitrary profile, *J. Geophys. Res.*, *90*, 11,917–11,927, 1985.

Dalrymple, R. A., A mechanism for rip current generation on an open coast, *J. Geophys. Res.*, *80*, 3485–3487, 1975.

Dalrymple, R. A., Rip currents and their causes, in *Coastal Engineering 1978: Proceedings of the 16th International Conference*, pp. 1414–1427, Am. Soc. of Civ. Eng., New York, 1978.

Dalrymple, R. A., Directional wavemaker theory with sidewall reflection, *J. Hydraul. Res.*, *27*, 23–34, 1989.

Dalrymple, R. A., and C. J. Lozano, Wave-current interaction models for rip currents, *J. Geophys. Res.*, *83*, 6063–6071, 1978.

Drønen, N., H. Karunarathna, J. Fredsøe, B. Mutlu Sumer, and R. Deigaard, The circulation over a longshore bar with rip channels, in *Coastal Sediments '99: Proceedings*, pp. 576–587, Am. Soc. of Civ. Eng., New York, 1999.

Falqués, A., A. Montoto, and D. Vila, A note on hydrodynamic instabilities and horizontal circulation in the surf zone, *J. Geophys. Res.*, *104*, 20,605–20,615, 1999.

Fowler, R. E., and R. A. Dalrymple, Wave group forced nearshore circulation, in *Coastal Engineering 1990: Proceedings of the 22nd International Conference*, edited by B. L. Edge, pp. 729–742, Am. Soc. of Civ. Eng., New York, 1990.

Garcez Faria, A. F., E. B. Thornton, T. C. Lippmann, and T. P. Stanton, Undertow over a barred beach, *J. Geophys. Res.*, *105*, 16,999–17,010, 2000.

Greenwood, B., and D. J. Sherman, Longshore current profiles and lateral mixing across the surfzone of a barred nearshore, *Coastal Eng.*, *10*, 149–168, 1986.

Haas, K. A., and I. A. Svendsen, Three-dimensional modeling of rip current system, *Tech. Rep. CACR-00-06*, Cent. for Appl. Coastal Res., Univ. of Del., Newark, 2000.

Haas, K. A., I. A. Svendsen, and M. C. Haller, Numerical modeling of nearshore circulation on a barred beach with rip channels, in *Coastal Engineering 1998: Proceedings of the 26th International Conference*, pp. 801–814, Am. Soc. of Civ. Eng., New York, 1998.

Haller, M. C., and R. A. Dalrymple, Rip current instabilities, *J. Fluid Mech.*, *433*, 161–192, 2001.

Haller, M. C., R. A. Dalrymple, and I. A. Svendsen, Experiments on rip currents and nearshore circulation: Data report, *Tech. Rep. CACR-00-04*, Cent. for Appl. Coastal Res. Univ. of Del., Newark, 2000.

Hamm, L., Directional nearshore wave propagation over a rip channel: An experiment, in *Coastal Engineering 1992: Proceedings of the 23rd International Conference*, pp. 226–239, Am. Soc. of Civ. Eng., New York, 1992.

Huntley, D. A., and A. D. Short, On the spacing between observed rip currents, *Coastal Eng.*, *17*, 211–225, 1992.

Longuet-Higgins, M. S., and R. W. Stewart, Radiation stress and mass transport in gravity waves, with application to "surf beats", *J. Fluid Mech.*, *13*, 481–504, 1962.

McKenzie, P., Rip-current systems, *J. Geol.*, *66*, 103–113, 1958.

Mei, C. C., and P. L.-F. Liu, Effects of topography on the circulation in and near the surf-zone–Linear theory, *Estuarine Coastal Mar. Sci.*, *5*, 25–37, 1977.

Putrevu, U., J. Oltman-Shay, and I. A. Svendsen, Effect of alongshore nonuniformities on longshore current predictions, *J. Geophys. Res.*, *100*, 16,119–16,130, 1995.

Raubenheimer, B., R. T. Guza, and S. Elgar, Field observations of wave-driven setdown and setup, *J. Geophys. Res.*, *106*, 4629–4638, 2001.

Reniers, A. J. H. M., and J. A. Battjes, A laboratory study of longshore currents over barred and non-barred beaches, *Coastal Eng.*, *30*, 1–22, 1997.

Reniers, A. J. H. M., E. B. Thornton, and T. C. Lippmann, Longshore currents over barred beaches, in *Coastal Dynamics '95: Proceedings of the International Conference on Coastal Research in Terms of Large Scale Experiments*, edited by W. R. Dally and R. B. Zeidler, pp. 413–424, Am. Soc. of Civ. Eng., New York, 1995.

Sancho, F. E., I. A. Svendsen, A. R. V. Dongeren, and U. Putrevu, Longshore nonuniformities of nearshore currents, in *Coastal Dynamics '95: Proceedings of the International Conference on Coastal Research in Terms of Large Scale Experiments*, edited by W. R. Dally and R. B. Zeidler, pp. 425–436, Am. Soc. of Civ. Eng., New York, 1995.

Shepard, F. P., and D. L. Inman, Nearshore circulation related to bottom topography and wave refraction, *Eos Trans. AGU*, *31*, 555–565, 1950.

Shepard, F. P., K. O. Emery, and E. C. La Fond, Rip currents: A process of geological importance, *J. Geol.*, *49*, 337–369, 1941.

Slinn, D. N., J. S. Allen, and R. A. Holman, Alongshore currents over variable beach topography, *J. Geophys. Res.*, *105*, 16,971–16,998, 2000.

Smith, J. M., M. Larson, and N. C. Kraus, Longshore current on a barred beach: Field measurements and calculation, *J. Geophys. Res.*, *98*, 22,717–22,731, 1993.

Sonu, C. J., Field observation of nearshore circulation and meandering currents, *J. Geophys. Res.*, *77*, 3232–3247, 1972.

Svendsen, I. A., Wave heights and set-up in a surf zone, *Coastal Eng.*, *8*, 303–329, 1984.

Svendsen, I. A., and J. Buhr Hansen, The interaction of waves and currents over a longshore bar, in *Coastal Engineering 1986: Proceedings of the 20th International Conference*, pp. 1580–1594, Am. Soc. of Civ. Eng., New York, 1986.

Svendsen, I. A., and U. Putrevu, Nearshore mixing and dispersion, *Proc. R. Soc. London, Ser. A*, *445*, 561–576, 1994.

Svendsen, I. A., K. A. Haas, and Q. Zhao, Analysis of rip current systems, in *Coastal Engineering 2000: Proceedings of the 27th International Conference*, edited by B. L. Edge, pp. 1127–1140, Am. Soc. of Civ. Eng., New York, 1999.

Wright, L. D., and A. D. Short, Morphodynamic variability of surf zones and beaches: A synthesis, *Mar. Geol.*, *56*, 93–118, 1984.

R. A. Dalrymple and I. A. Svendsen, Center for Applied Coastal Research, University of Delaware, Newark, DE 19716, USA.

M. C. Haller, Department of Civil, Construction, and Environmental Engineering, Oregon State University, 202 Apperson Hall, Corvallis, OR 97331-2302, USA. (hallerm@engr.orst.edu)